Doctoral Dissertation
博士論文

Laser Excitation of Confined Positronium in Porous Materials for Rapid Cooling

（高速冷却を目指した多孔質材料中におけるポジトロニウムのレーザー励起）

A Dissertation Submitted for the Degree of Doctor of Philosophy
December 2019

令和元年 12 月博士（理学） 申請

Department of Physics, Graduate School of Science,
The University of Tokyo
東京大学大学院理学系研究科
物理学専攻

Kenji Shu
周 健治

Abstract

Rapid cooling of positronium (Ps) is an essential technique to improve precision of testing fundamental theories, and to realize the first Bose-Einstein condensation with antimatters. It was recently proposed that Doppler laser cooling of Ps confined in a porous material is efficient enough to achieve such targets. In this process Ps is excited many times inside nano pores. It was, however, reported that decay of the excited Ps into annihilation γ-rays was enhanced in nano pores and a line width of the resonace was broadened, both of which make the proposed cooling method useless. In that report, the decay of Ps in the ground state was also enhanced by being possibly trapped at some contaminants remaining on the surface of the pores, and the origin of the abnormal phenomena was attributed to the formation of such surface state. In this thesis, a Ps confining cavity which did not have the contaminants affecting Ps in the ground state was fabricated, and laser excitations of Ps in the pores were performed. The excited Ps had the similar enhancement of the decay and broad resonance spectrum also in the new cavity to favor that some of the distinctive features of the excited state, such as the small binding energy or high electric susceptibility, are origins of the abnormal phenomena. In order to quantitativaly estimate the decay rate and the broadening effect of the excited Ps, a realistic model was newly constructed with including those parameters. It was measured for the first time that the decay rate was in the order of 1 THz and depended on kinetic energy of Ps. The width of the resonance spectrum was broadened as wide as 1 nm in FWHM but independent on the decay rate. This favors that the broadening is induced by other machanisms from the enhanced decay. Possible mechanisms of both of the enhanced decay and the broadening , and future works to elucidate them are discussed following the measurements.

Contents

List of Figures

List of Tables

Chapter 1

Introduction

Positronium (Ps), which is a bound state of an electron and a positron, is an excellent system to study fundamental physics. One of the breakthroughs for the study is to develop an efficient method of cooling Ps down to several Kelvins. I and the collaborators proposed a new method which combined thermalization processes and Doppler laser cooling for Ps confined in a porous material [1]. Excitations of Ps into the 2P state in the pores must be repeated many times in the method, but a recent experiment reported that the cycle would be impossible because confined Ps in nano pores of silica (SiO_2) rapidly decayed into annihilation γ-rays by the excitation, and the width of the resonance spectrum was abnormally broadened [2]. Mechanisms of this enhanced decay and the broadening have been totally unknown while it was suggested that Ps formed a state strongly affected by the material and this state had the large decay rate when excited into the 2P state. The formation of the state was assumed by disagreements between measured lifetimes of confined Ps in the 1S ground state (1S-Ps) and conventional models. It is necessary to elucidate the mechanisms of the enhanced decay and the broadening to develop a new Ps confining cavity which is able to be used for the method of cooling. The present work aims to test the proposed assumption by exciting Ps into the 2P state (2P-Ps) confined in a silica aerogel, in which the decay rate of 1S-Ps agreed with the conventional model, and to quantitatively measure the decay rate and the width of the resonance of 2P-Ps to provide clues for identifying physical processes of the abnormal phenomena.

1.1   Properties of positronium

Positronium (Ps) is a bound state of an electron and a positron. It has been an excellent system for studying fundamental physics thanks to its simple and exotic composition. Ps consists of only leptons so that precise tests of Quantum Electrodynamics (QED) have been performed [3] through calculations and measurements of decay rates [4–7] and various energy intervals of internal states [8–10]. The exotic feature that Ps consists of the pair of the matter and antimatter has allowed to search for CP violation in the lepton sector [11] and exotic decays mediated by new physics beyond the Standard Model [12–14].

1
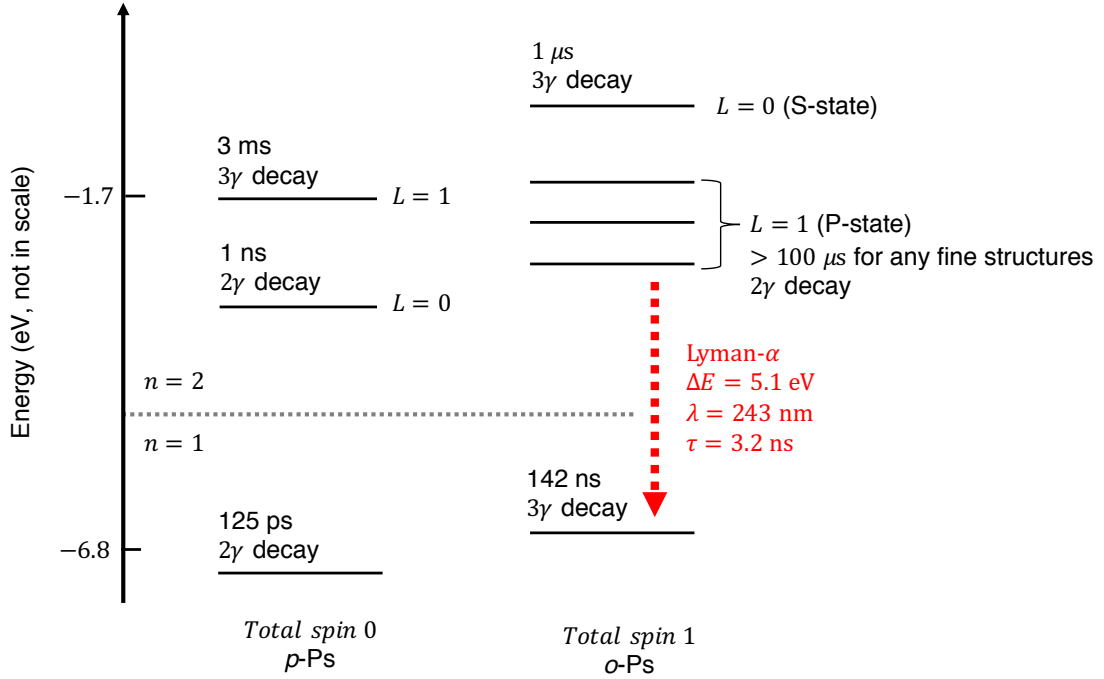
Figure 1.1: Properties of Ps in various internal states. Decay modes, lifetimes, and details of the Lyman-α transition are noted. L represents the azimuthal quantum number for the orbital angular momentum.

1.1.1 Internal states and decay modes

Ps has various decay rates and modes into annihilation γ-rays depending on its internal structures. Main decay modes are 2γ decay into mono energetic 511 keV γ-rays in back-to-back directions, and 3γ decay in which γ-rays with continuous energy spectra are resulted. Decay modes are determined by C and P symmetry, and the decay rates depend on scattering amplitudes to each mode and overlaps of the eigen wave functions of the positron and the electron. Figure 1.1 summarizes the decay modes and lifetimes for the principal quantum number $n = 1$ and 2 [15–18]. Features of o-Ps in the 1S ($n = 1$, $L = 0$) and the 2P ($n = 2$, $L = 1$) states are important for the present work. Ps represents o-Ps hereafter if not specified. Observations of the long lifetime and the continuous energy spectrum of annihilation γ-rays can be evidences of productions of o-Ps in the 1S state. 2P-Ps have very long lifetimes for self annihilations, but the short lifetime (3.2 ns) of the spontaneous decay into the 1S state. The Lyman-α transition of Ps can be induced by 243 nm UV light, and is the best transition for laser cooling because of the short lifetime and availability of a laser system at the wavelength.

State with low center of motion energy
→ Small overlap, less pick-off decay

State with high center of motion energy
→ Large overlap, more pick-off decay
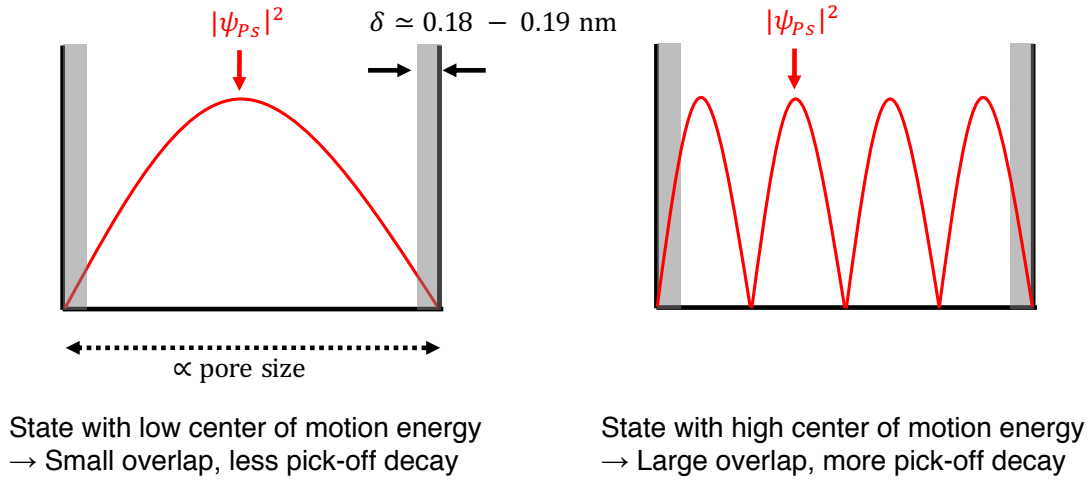
Figure 1.2: Schematic description of the RTE model. Pore surfaces are modeled as infinite potential barriers. Overlaps between the probability amplitude and the thin skin region from the surfaces ($\delta \simeq 0.18\,\mathrm{nm}$) determine the pick-off decay rate.

1.1.2 Interactions with material

Ps can be produced by irradiating a positron to suitable materials. Silica (SiO_2) is one of the materials with high Ps production probability [19]. Materials also affect produced Ps through various interactions to result in variations of the lifetime and kinetic energy. Information of Ps can be obtained by measuring those effects. Major interactions related to the present work are introduced hereafter.

Pick-off decay

The lifetime of 1S-Ps in materials depends on sizes of internal pores or voids if exist because the pair annihilations occur between the positron in Ps and an electron in the material. This decay process is called pick-off decay [20, 21], and dependences of the pick-off decay rate on pore size and kinetic energy of Ps can be predicted by so-called Rectangular Tao-Eldrup (RTE) model [22, 23]. Figure 1.2 shows a schematic description of the model. In the RTE model, pore surfaces are modeled as infinite potential barrier, and the distances between barriers are determined so that a mean free path in pores of the material is reproduced. The RTE model assumes a rectangular shape for the space surrounded by the barriers. The pick-off decay rate can be calculated by assuming that Ps has a spin-averaged decay rate ($0.25/125\,\mathrm{ps} + 0.75/142\,\mathrm{ns}$) if it exists within the distance of $\delta \simeq 0.18\,\mathrm{nm}$ from the barriers. The model can be considered to be valid for materials which have a negative work function for Ps, such as silica with around $-1\,\mathrm{eV}$ because the negative work function validates the picture that Ps behaves like free particle in the square well potential without strongly affected by the material. An agreement between a measured lifetime of 1S-Ps and the prediction by the RTE model is a good signature that 1S-Ps

3

(a) In lifetimes.　　　　　　　　　　(b) In decay rates.
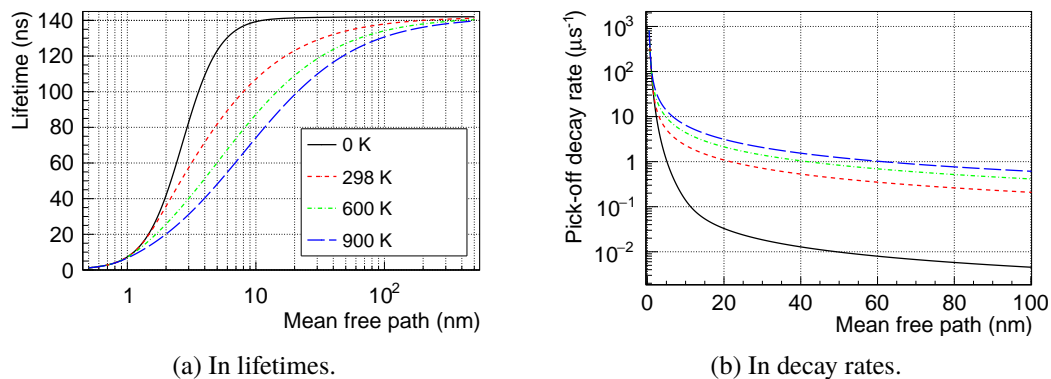
Figure 1.3: Dependence of the pick-off decay rate on mean free path for various temperatures of Ps.

is not bounded to the surface.

In the previous work [2], the possible formations of the state which were bounded to the surface of the pores were assumed from shorter lifetimes of 1S-Ps than the predictions of the RTE model.

Formations of the surface state, which is the suspected origin of the abnormal behaviors of 2P-Ps, would be verified through measurements of the pick-off decay rate in the present work.

The pick-off decay rate depends on kinetic energy of Ps and pore sizes because the overlapping ratio between Ps wave function and the thin skin (δ) from the surfaces depends on those parameters. δ was empirically determined to reproduce measured lifetimes of o-Ps in pores whose sizes were able to be assumed by other methods. Figure 1.3 show dependence of lifetimes and the corresponding pick-off decay rates on mean free path for various temperatures of Ps. The pick-off decay will also occur even for stopped Ps with $0\,\mathrm{K}$ because it is impossible for particle to be fully localized away from the surface in the quantum mechanics. This quantum effect is significant especially for Ps, whose small mass leads to a large de Broglie wave length ($\lambda_{Ps}^{dB} = 0.87\,\mathrm{nm}\sqrt{1\,\mathrm{eV}/E_{Ps}}$). The pick-off decay rate can be approximated by a linear function on kinetic energy or temperature of Ps if the quantum effect is small [22]. Figure 1.4 show dependences of the pick-off decay rate on temperature of Ps with and without the approximation for a mean free path of $40\,\mathrm{nm}$. Both results agree in $10\,\%$ accuracy at more than $50\,\mathrm{K}$ for the mean free path.

Spin exchange interactions

Spin exchange interactions, in which the spin of a consisting particle in o-Ps is flipped to form p-Ps, also decrease the effective lifetime of o-Ps because p-Ps has much less lifetime [24–26]. This quenching interactions can be occurred between paramagnetic radicals which can be induced by irradiation of UV light on the material. It was demonstrated for silica based materials that the productions of the radicals could be suppressed by proper treatments of chemical groups on the surface of the material [24].

4
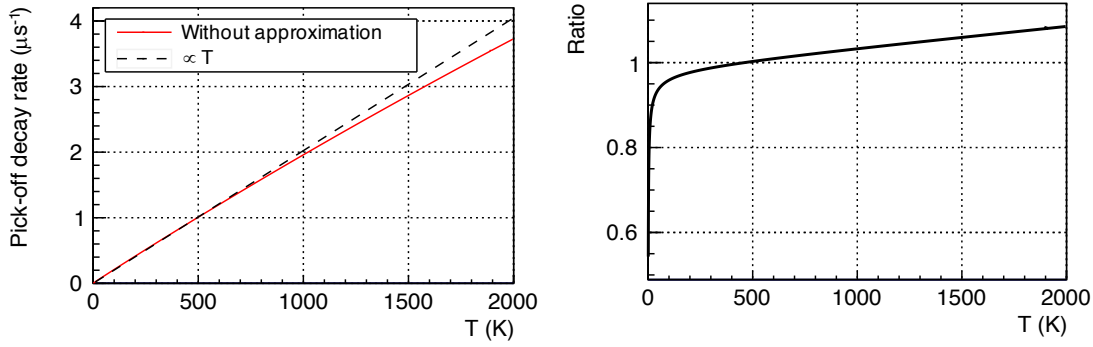
Figure 1.4: (Left) Dependences of the pick-off decay rate on temperature of Ps with and without the approximation. (Right) Ratio of the results. Both results agree in 10% accuracy at more than $50\,\mathrm{K}$.

Thermalization

Ps is thermalized to temperature of the surrounding material through energy exchanging processes. From an initial temperature around $10\,000\,\mathrm{K}$, which is determined from work functions of the material for Ps, this thermalization process typically takes the same order of time as the lifetime of o-Ps. Time evolution of kinetic energy of Ps, E, can be modeled by a classical elastic collision model [27] as

$$\frac{\mathrm{d}E}{\mathrm{d}t} = -\frac{2}{LM}\sqrt{2m_{\mathrm{Ps}}E}\left(E - \frac{3}{2}k_BT\right), \tag{1.1}$$

where L is a mean free path of collisions, M is a mass of bodies to be collided with, m_{Ps} is the mass of Ps, k_B is the Boltzmann constant, and T is a temperature of the surrounding material. It was also suggested that an introduction of dependence of M on E would enable to describe the thermalization process in a wide range of E where inelastic scatterings or quantum size effects took effect. I and collaborators measured time evolutions of temperature of Ps confined in a silica aerogel, which is a highly porous material made by silica, at cryogenic temperatures [28, 29]. Figure 1.5 shows the results of the measurements. The process in which Ps lost its kinetic energy was clearly observed. L was estimated as around $40\,\mathrm{nm}$ by the gas adsorption measurement. Temperatures of Ps were evaluated by the pick-off decay rates ($\langle\Gamma_{po}\rangle$) averaged in each timing windows. The conversion from $\langle\Gamma_{po}\rangle$ to temperature of Ps was performed according to the RTE model. The vertical axis shows the ratio of $\langle\Gamma_{po}\rangle$ over the self decay rate Γ_s of o-Ps. The time evolutions were able to be reproduced by introducing the dependence of M on E. Time evolution of kinetic energy of Ps is estimated according to these measurements in the present work.

5
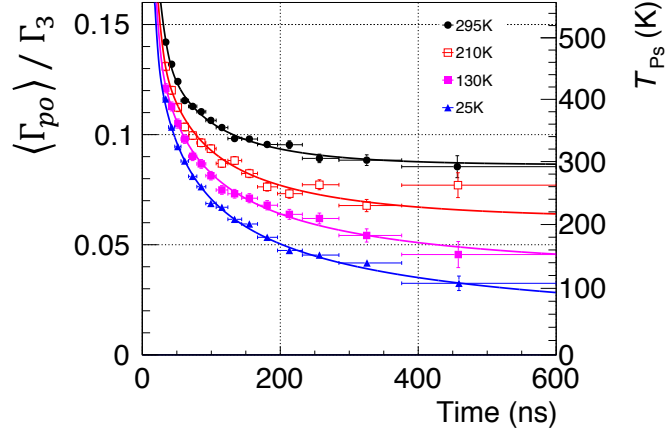
Figure 1.5: Time evolution of temperature of Ps in the silica aerogel. Legends in the figure show temperatures of the aerogel. The temperatures of Ps were evaluated by the pick-off decay rates at each timing window.

1.2 Cooling of Ps

1.2.1 Motivations

Cold Ps will be beneficial to advance the study on fundamental physics, and also be useful for industrial applications. A current target is to develop a method to cool Ps down to several Kelvins. This will enable to test CPT invariance and an existence of "antigravity", and to realize Bose–Einstein condensation of Ps.

Productions of cold Ps at less than 10 K will increase the precision of the spectroscopic measurement of the 1S–2S energy interval of o-Ps by an order of magnitude [30, 31]. As discussed in the work which measured the interval with the highest precision [9], the high Ps temperature around 600 K in the work contributed most significantly to the systematic uncertainty. The fast motion of Ps resulted in the large second order Doppler shift and short time duration while Ps interacted with laser fields. The latter effect required strong laser fields which inevitably caused large AC Stark shift, and also led to large transient broadening. The medium velocity of Ps will be reduced by around factor 8 through the cooling. It was estimated that the systematic uncertainty would be reduced by around an order of magnitude. With the improved precision, the mass difference of a positron and an electron, which would arise if CPT invariance was broken, will be measured in the highest precision by measuring the interval [9, 32]. The improvement will be also large enough to test a tiny shift on the interval which would be caused by hypothetical repulsive gravitational force between the earth and a positron if assumed that antimatters had the negative gravitational mass whose absolute was same as the inertial mass. This "antigravity" could possibly explain the accelerating expansion of the universe without introducing the dark energy [33], while the ideas are still theoretically controversial [34, 35].

A realization of Bose–Einstein condensation (BEC) of Ps is another desirable application in which the cold Ps plays a critical role. Ps is one of the most promising systems to realize the first
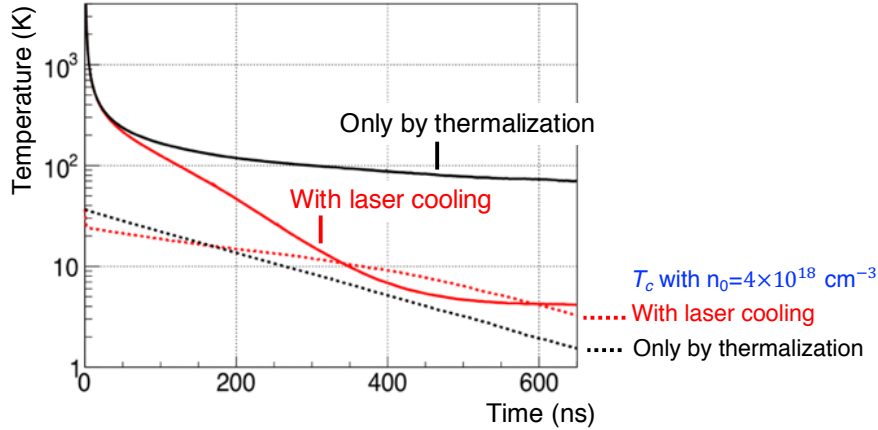
Figure 1.6: Simulated time evolutions of temperature of Ps and the critical temperature T_c of the BEC transition under the new scheme of the cooling. The BEC transition will be observed at around 300 ns later from the productions of Ps with the initial density of 4×10^{18} cm^{-3}. The remained density with the laser was higher than that without the laser because of the long annihilation lifetime of the 2P states.

BEC with antimatters [36] because of the following two merits for achieving the high enough phase space density necessary to cause the BEC transition:

1. High critical temperature as 14 K at 10^{18} cm^{-3} thanks to its light mass.

2. Availability of producing a denser cloud of Ps than any other systems with antimatters.

Cooling of Ps down to several Kelvins has been under intense study [1, 37] because recent progresses of positron accumulation [38, 39] and focusing [40, 41] suggested that a dense Ps as 10^{17} cm^{-3}–10^{18} cm^{-3} would be available in the near future. Ps-BEC will be an antimatter laser which can be used for a Mach–Zehnder interferometer. The sensitivity of the interferometer will be largely increased by the high coherence of the BEC state so that the gravity effect on Ps will be measured [42]. Another unique application by Ps-BEC is to generate 511 keV γ-ray laser [43, 44]. High coherence of the γ-rays is expected thanks to collective decays from the BEC state. The γ-ray laser can be used for such as non destructive inspections of infrastructures.

1.2.2 New method of rapid cooling

I proposed a new method of efficient cooling [1] combining the thermalization process and Doppler laser cooling. Ps will be produced inside a porous silica material at cryogenic temperature, and be efficiently cooled down to around 200 K through the thermalization process. A 243 nm UV laser which induces the Lyman-α transitions will be irradiated on Ps in the material for Doppler cooling. Figure 1.6 shows simulated time evolutions of temperature of Ps and the critical temperature T_c of the BEC transition. A pore size was set to be 75 nm in the simulation.

The laser accelerate cooling from around 200 K and be efficient enough to cool Ps down to less than 10 K in 350 ns from the productions of Ps. The BEC transition would be observed thanks to both of the efficient cooling and the extended annihilation lifetime of the 2P states if an initial density as high as $4 \times 10^{18}\,\mathrm{cm}^{-3}$ was achieved. An essence of the method is to perform laser cooling on confined Ps: this will bring two merits as (1) the two processes can efficiently cool down Ps in the wide range of its kinetic energy, and (2) Ps can stay with a spot of the laser irradiation by the confinement without which it escapes with large velocity.

1.3 Enhanced decay and broadening effect of confined 2P-Ps

1.3.1 Observations with porous silica material which affected 1S-Ps

The key process in the cooling method is to repeat the cycle of the Lyman-α transitions for Ps confined in nano pores, but effects on 2P-Ps by the material are not understood well. The first experimental demonstration of the Lyman-α transition of confined Ps was reported in 2011 [45]. For Ps confined in a porous silica material with around 5 nm pores, they observed a blue shift of center and a narrowed width of the resonance spectrum. The shift was attributed to some effects from the material, and the narrowing to Dicke effect [46], which suppresses Doppler broadening. It was expected that large pores would ease those effects, but another work in 2018 reported that the width was conversely broadened and 2P-Ps immediately decayed into γ-rays in pores as large as 75 nm [2]. The broadened width was as wide as 2 nm in the wavelength (10 THz in the frequency), which was too wide to be attributed to any known phenomena including Doppler or the collisional broadening. Both of the effects make the proposed cooling method useless because the wide width inhibits Doppler shift which is used in laser cooling to selectively excite the counter propagating Ps against to the laser, and the enhanced decay largely decreases the remained number of Ps after the cycles of the Lyman-α transitions.

Mechanisms of the broadening effect and the enhanced decay must be elucidated, but only limited information is available. One of the important observations in the previous work was that measured lifetimes in the porous silica materials were shorter than the predictions by the RTE model. The lifetimes were almost independent on pore sizes ranging from 5 to 75 nm for their four samples. They suggested that the short lifetimes originated from formations of bound states between Ps and the surfaces of the pores. The formations of the surface state were assumed to be induced by some contaminants remaining at isolated pores because the two effects were not observed in 2011's work, which used a porous silica whose pores connected each other.

1.3.2 Aims of the present work

Following the observations, the present work has two main aims. The first one is to test the assumption that the surface state induced the broadening effect and the enhanced decay by using another type of porous silica material in which Ps is not bounded to the surface states in the 1S state. Silica aerogels are used since lifetimes of 1S-Ps in those pores agree with the predictions by the RTE model. This agreement favors that Ps moves almost freely in pores rather than being bound to the surfaces. In the present work, Ps is produced in well characterized aerogels and excited into the 2P state to investigate whether the broadening and the enhanced decay are

observed even without being bounded to the surface in the 1S state. The decay rate of 2P-Ps is also quantitatively estimated by applying a realistic model which includes the decay rate to measured intensities of annihilation γ-rays. A dependence of the decay rate on kinetic energy of Ps is also measured by changing timings of the laser irradiation. This is possible because kinetic energy of Ps varies time by time through the thermalization process. The measured decay rate will be useful information to identify physical processes to induce the abnormal behaviors of 2P-Ps.

Chapter 2

Experimental Setup

Experiments were conducted at Slow Positron Facility (SPF) in High Energy Accelerator Research Organization (KEK) [47]. A dedicated setup at the B1 beam line of KEK-SPF was build to measure the decay rate of 2P-Ps which were confined in a silica aerogel. The setup mainly consisted of four parts:

1. Positron supplier. KEK-SPF supplied bunched positrons in a short pulse.

2. Positronium converter. It supplied electrons to the irradiated positrons to form Ps. Ps might be trapped in pore networks of the converter.

3. Laser system. Pulse lasers were synchronized with the positrons to be irradiated on the produced Ps. The lasers were used to excite Ps to the 2P state, and then possibly ionizing 2P-Ps into a dissociated positron and an electron.

4. γ-ray detector. Annihilation γ-rays were detected to measure the decay rates of Ps.

Figure 2.1 shows a picture of the setup. Figure 2.2 show drawings of a vacuum chamber to perform laser excitations of Ps confined in the Ps converter. Pressure in the vacuum was kept less than 5×10^{-6} Pa. Each part is introduced in the following sections.

2.1 Positron supplier

Bunched positrons in short pulses can be supplied at KEK-SPF. Its shortness of the pulse duration is an essential requirement to be synchronized with the pulse laser system. Table 2.1 summarizes beam properties used in the experiments. The methods to evaluate the parameters are introduced in the following paragraphs. A brief review of KEK-SPF, and modifications applied on the positron beam are introduced in the following subsections.

Intensity The intensity of the positrons at the Ps converter was estimated by that of annihilation γ-rays measured by the detector, which is described in detail in section 2.4.
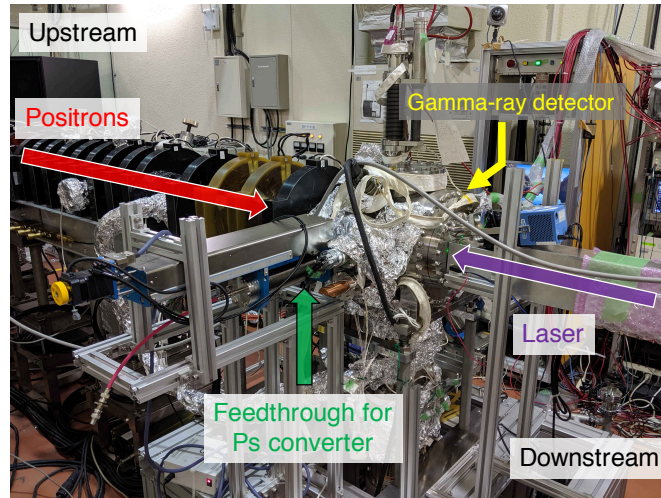
Figure 2.1: Picture of the experimental setup.
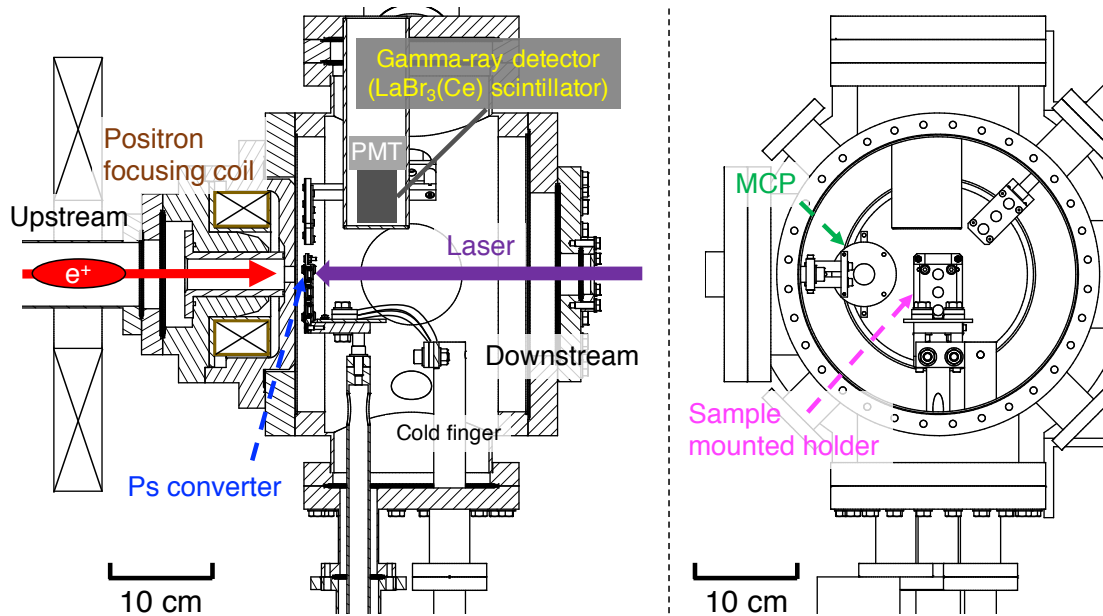
Figure 2.2: Drawings of the experimental chamber to excite Ps confined in the Ps converter. (Left) Cross sectional drawing of the chamber. (Right) Drawing inside the chamber from the downstream of the beam line.

Table 2.1: Properties of the positron beam. The intensity was estimated by that of annihilation γ-rays. The timing and spacial profile were evaluated by the MCP.

Energy	5 keV
Intensity at Ps converter	$1 \times 10^5 \text{ s}^{-1}$
Pulse time duration	11 ns FWHM
Beam size	2.6 mm FWHM
Repetition	50 Hz
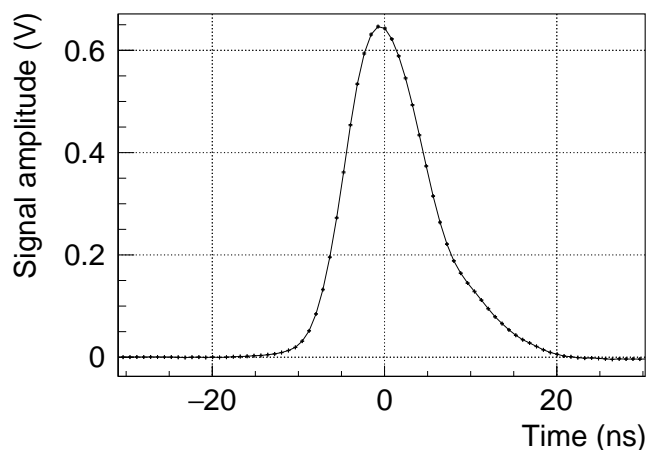
Figure 2.3: Timing profile of the positron pulse measured by the MCP. Waveforms were averaged over one minute data acquisition.

Timing profile   The timing profile of the positron pulse was measured by a Micro-Channel Plate (MCP, HAMAMATSU, F2222-21P). Figure 2.3 shows an averaged profile in one minute. FWHM of the pulse was measured to be 11 ns. The signal was amplified by a fast preamplifier (ORTEC, VT120C).

Spacial profile   The spacial profile was measured by imaging the phosphor screen of the MCP at a position of the Ps converter. Figure 2.4 shows the spacial profile imaged by a CCD camera. The beam size was estimated as 2.6 mm FWHM by fitting the profile by a 2D-Gaussian function. The positron beam was focused by a magnetic lens, which is described in subsection 2.1.3.

2.1.1   Accelerator based slow positron production

KEK-SPF produces slow positron beams using a linear accelerator (LINAC) [47]. Positrons are generated by pair creation processes from bremsstrahlung γ-rays. The γ-rays are emitted by shooting electrons which are accelerated by the LINAC into a tantalum converter. The positrons are re-moderated by tungsten meshes to have kinetic energy of around 3 eV, which is determined
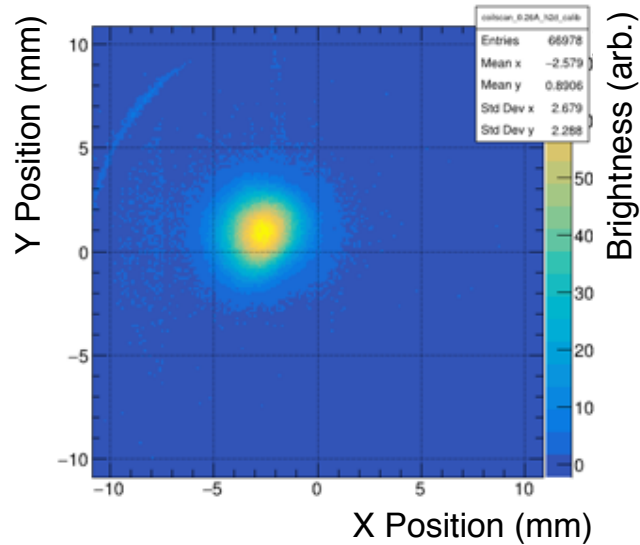
Figure 2.4: Spacial profile of the positron beam. The image was averaged over one minute data acquisition.

by a work function of tungsten for positrons. This converter/moderator system was biased to 5 kV so that the 5 keV positron beam could be obtained at experimental spaces in the ground potential. The positron beam was guided to the experimental chamber for around 10 m by an axial magnetic field generated by solenoid coils.

2.1.2 Retarding bias to block slower positrons' contamination

Retarding high voltage bias was applied to block slower positrons which would arrive at the chamber later than the main pulse of the beam. In order to reflect the slower positrons to the upstream, a blocker with three plates were introduced before the experimental chamber. Figure 2.20 shows a drawing including the blocker assembly. The blocker assembly was placed around 80 cm ahead from the position of the Ps converter. The three plates in the assembly had a 30 mm aperture. Each aperture was covered by a tungsten mesh (30 μm for wires' diameter, 93 % opening) to uniformly apply electric field. The plates were placed in parallel to each other, and the center plate was biased to 3.5 kV. The others were in the ground potential. Positrons with lower energy than 3.5 keV are reflected to the upstream, but those with higher energy pass through the assembly with retaining the original energy. The bias voltage was determined to achieve the best signal-to-noise ratio.

2.1.3 Magnetic focus lens

The positron beam, whose diameter was initially around 20 mm, was focused on the Ps converter to increase an overlap with the laser (6 mm FWHM size). A magnetic lens which consisted of

14

To upstream

The blocker assembly

Biased plate

Solenoid coils

20 cm
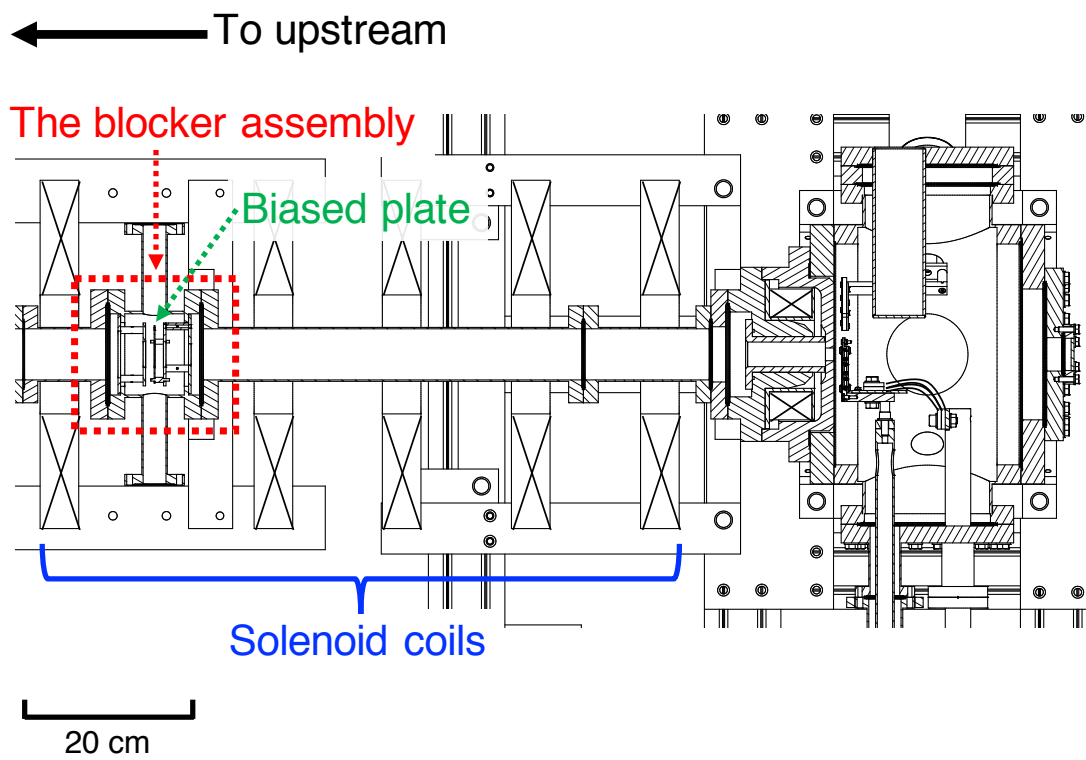
Figure 2.5: Drawing including the blocker of the slower positrons. The plate at the center of the blocker assembly was biased in high voltage.
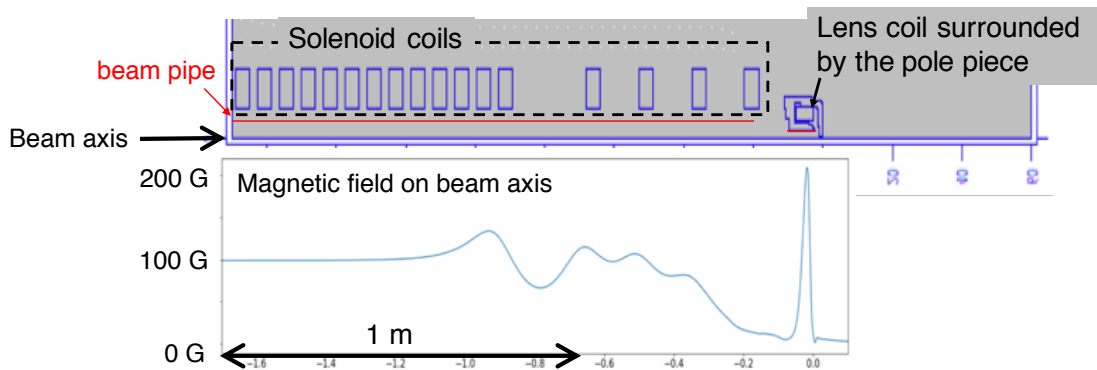
Figure 2.6: Configuration and magnetic field of positron focusing. The geometry is shown by cross sectional view and had the rotational symmetry around the beam axis.

a solenoid coil and a pole piece was installed. It generated concentrated magnetic field which focused positrons by Lorentz force. Figure 2.6 shows a coil configuration including the lens and the guiding solenoid coils, and calculated magnetic field on the beam axis by inputting currents actually flowed. The currents were optimized to achieve the highest intensity in the spot size of the laser. The resulted beam had the reasonable size assumed by the initial beam size, energy spreading of the beam, and a performance of the lens.

2.2 Positronium converter

Silica aerogels were used as the positron-to-positronium converter and Ps confining cavity in the present work. Aerogels have open pore networks with high porosities where Ps can be emitted with high probability. A non-porous silica thin film was deposited to cap the pore network to prevent Ps from escaping into the outer vacuum. Decay rates of o-Ps inside the pores were measured to be consistent with the RTE model. This agreement indicates that 1S-Ps is not bounded to the surface and moves almost freely in the pores of the aerogel. It is then possible to test the assumption of the previous work [2] that the strong material effect by which 1S-Ps is bounded on the surface is the origin of the enhanced decay of 2P-Ps and the broad resonance spectrum. The following sections describe production processes and examined properties of the silica aerogel cavities.

2.2.1 Silica aerogel

Silica aerogels used in the experiments were supplied by Japan Fine Ceramics Center. Properties of the aerogels are summarized in Table 2.2. The thin shape was fabricated in custom for the present work to suppress a energy loss of the laser which was irradiated on Ps after transmitting the aerogel.

16

Table 2.2: Properties of the silica aerogel used in the experiments. The mean free path was calculated by the pore diameters assuming sphere shapes for pores.

Product name	SP-30
Surface chemical groups	$SiOCH_3$ (hydrophobic)
Density	$0.12\,\mathrm{g\,cm^{-3}}$
Pore diameters	40 nm–50 nm
Mean free path	30 nm–37.5 nm
Porosity	95%
Thickness	0.5 mm

2.2.2 Measurement of Ps lifetime in the aerogel

The decay rate of 1S-Ps confined inside the pore network of the aerogel was measured to check the consistency with the RTE model. A Na-22 radioisotope was used as a positron source for this measurement. Figure 2.7 shows an acquired timing spectrum. Two silica aerogels with 1 mm thickness sandwiched the source in this measurement. The origin of the timing was determined by detecting 1275 keV γ-ray from Na-22 which is followed by the beta decay. A background by accidental hits was subtracted. A decay rate of thermalized Ps was measured by fitting a exponential function to the timing spectrum from 180 ns. The fitted curve is superimposed in Figure 2.7. The acquired life time was 131 ± 2 ns ($0.6 \pm 0.1\,\mathrm{\mu s^{-1}}$ in the pick-off decay rate) and agreed with the prediction for the mean free path of 30 nm–37.5 nm by the RTE model as shown in Figure 1.3. This agreement favored that the assumed picture of the RTE model was valid in the aerogels and 1S-Ps did not form the surface state through strong effects by the material. An intensity of the o-Ps component was 13 % in the spectrum. A production probability of Ps was estimated as around 35 % by including mean stopping probability in the aerogels, detection efficiency for 2γ decay from the prompt components and 3γ from o-Ps, and spin statistics for p-Ps and o-Ps. This efficient production was reasonable for aerogels with high porosity.

2.2.3 Capping by non-porous silica film

The top surface of the aerogel from which the positrons were irradiated was capped by a thin non-porous silica film to prevent Ps from escaping. The thickness of the film was confirmed to be 75 nm by ellipsometry measurements of silicon wafers which were capped beside the aerogel. Around 70 % of the positrons with 5 keV energy was expected to penetrate the film to reach the pore network of the aerogel. The capping was conducted by the plasma enhanced chemical vapor deposition (PE-CVD) process. Tetraethyl orthosilicate ($Si(OC_2H_5)_4$, TEOS) and oxygen (O_2) gasses were mixed to be used as base materials for the SiO_2 film. Capping parameters are listed in Table 2.3
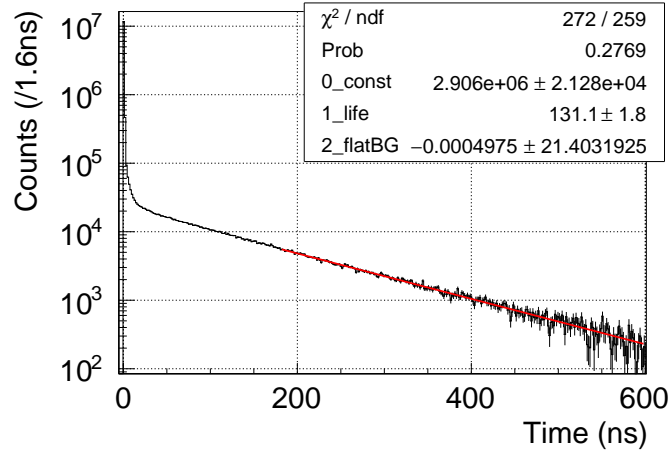
Figure 2.7: Timing spectrum of annihilation γ-rays from Ps in the aerogel using Na-22. The measured lifetime agreed with the prediction from the RTE model. It implies that 1S-Ps is not bounded to the surface of the silica aerogel.

Table 2.3: Parameters of CVD process for non-porous silica capping

TEOS gas flow	10 sccm
O_2 gas flow	400 sccm
Deposition time	110 s
Substrate temperature	120 °C

18
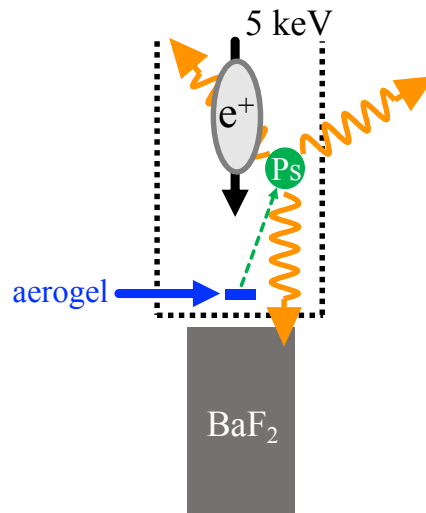
Figure 2.8: Schematic view of a geometrical configuration to confirm the confinement of Ps. The BaF$_2$ detector had less detection efficiency for escaped Ps so the lifetime would become spuriously short by the escape.

2.2.4 Ps confinement by the capping

The confinement of Ps by the cap was confirmed by lifetime measurements using a slow positron beam at National Institute of Advanced Industrial Science and Technology (AIST). A geometry of the measurement was set up as shown in Figure 2.8 to be sensitive for the escape of Ps into the outer vacuum of the aerogel pores. Positrons at the beam line of AIST are supplied by LINAC based pair productions, and then timing of their irradiation is controlled by a electric chopper. If Ps produced in the aerogel escaped, a decay component with a spuriously short lifetime would be obtained because the BaF$_2$ detector had lower detection efficiency for escaped Ps. Figure 2.9 compares timing spectra of annihilation γ-rays obtained by aerogels with and without the cap. The origin of the timing was determined by triggers of the chopper. The lifetime was spuriously short without the cap by the escape, but the cap recovered the lifetime to the same value as measured in the bulk. The confinement of Ps was successfully demonstrated.

2.2.5 Mount on sample holder

Samples including the aerogels with and without the cap were mounted on the holder with sandwiched by the tungsten mesh and plates with a 10 mm aperture. Figure 2.10 shows a magnified drawing around a sample holder. The mesh was put to prevent possible charge up of the samples by the positron irradiations. The samples were pressed by four spring coils which were attached to the plates to realize better contact with the mesh and the holder. The weight was 400 gf per coil. A kapton film, which is a polyimide film fabricated by Du Pont company, was also mounted for calibration measurements since simple analysis was possible due to less formation of Ps inside it.
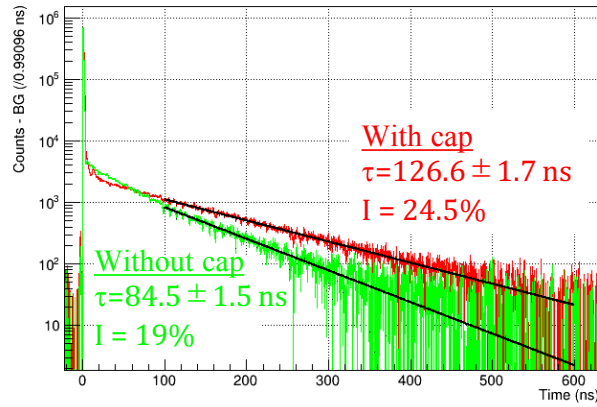
Figure 2.9: Timing spectra of annihilation γ-rays obtained by aerogels with and without the cap. With the cap, the lifetime was recovered to the same value as measured in the bulk by confinement.
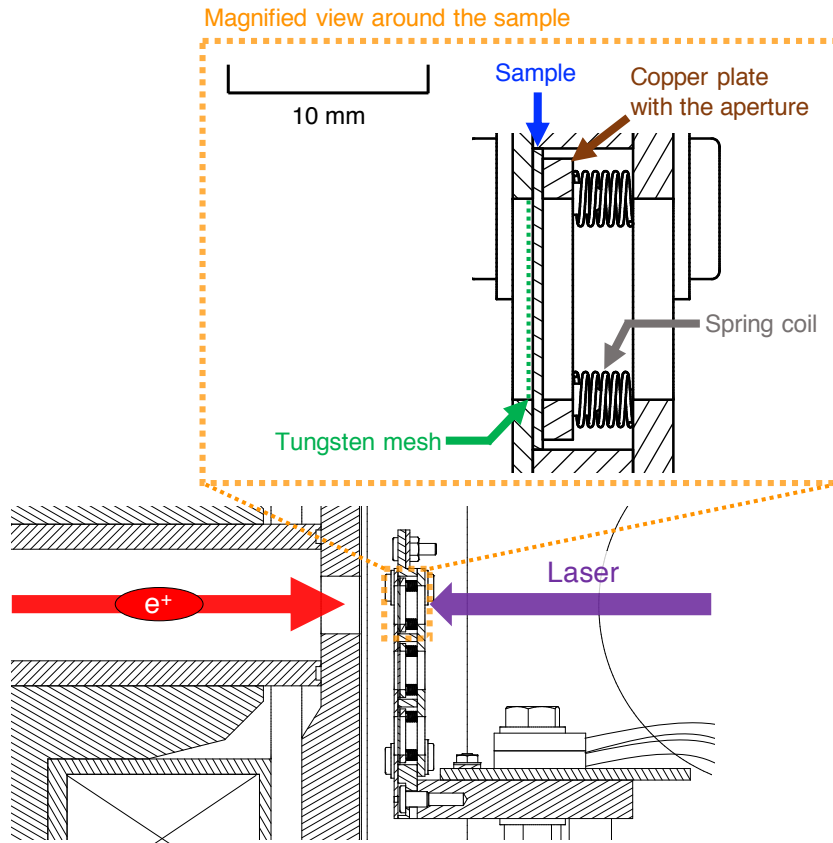
Figure 2.10: Magnified drawing around the sample holder. The samples were sandwiched and pressed by the tungsten mesh and copper plates with a 10 mm aperture.

20
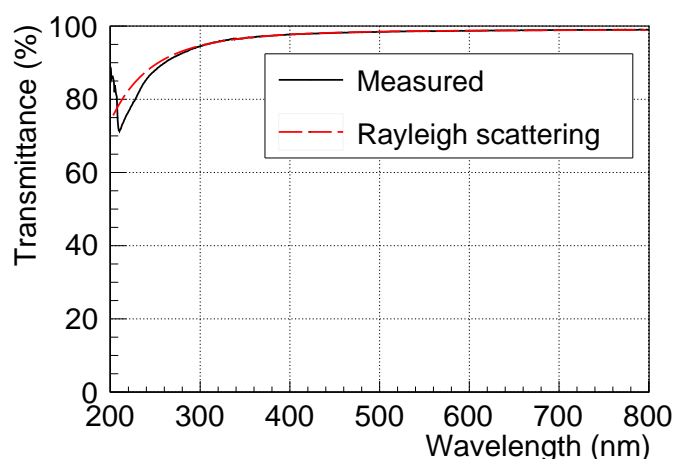
Figure 2.11: Optical transmittance of silica aerogel. The dependence on wavelength down to 300 nm was able to be described well by Rayleigh scatterings. 85 % of 243 nm light transmitted the sample.

2.2.6 Optical properties

Optical transmittance and absorption of the aerogel were studied because the laser was also irradiated on the aerogel to excite confined Ps. Figure 2.11 shows an optical transmittance of the aerogel measured by a spectrophotometer (JASCO, V-770). High enough transmittance as 85 % for 243 nm light, which is the Lyman-α wavelength of Ps, was achieved for the thin aerogel adopted in the present work. Transmittance down to 300 nm was well described by dependence of Rayleigh scatterings ($\exp(-\lambda^{-4})$) as superimposed in the figure.

Absorptions and following fluorescence were observed in UV region. Figure 2.12 shows a picture of the aerogel irradiated by laser with 243 nm wavelength. Fluorescence by UV laser irradiation was observed while 243 nm light is invisible for human eyes. Other materials made by silica, such as a view port window or a wafer, also exhibited the similar fluorescence. These could be originated from impurities in silica or multi-photon processes. Intensities of the fluorescence excited by UV lights were measured by a spectro fluorometer (JASCO, FP-8500). Figure 2.13 shows intensities of fluorescence lights excited by UV light whose wavelength was scanned from 233 to 253 nm. Four peaks were observed and the intensity of each peak was measured by scanning the excitation wavelength. The results of the scan are shown in Figure 2.14. Bandwidths of the excitation light were expected to be 2.5 nm, and wavelength accuracy 1 nm by the device's specification. No peak was observed at the wavelength of Ps Lyman-α (243 nm). If the enhanced decay of Ps was observed, the presence of the resonance would be able to determine whether the decay was induced by Ps Lyman-α transitions or some phenomena related with the light absorptions.
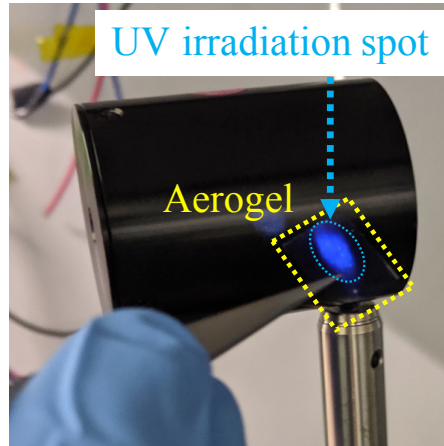
Figure 2.12: Picture of the aerogel showing blue fluorescence by UV laser irradiation.
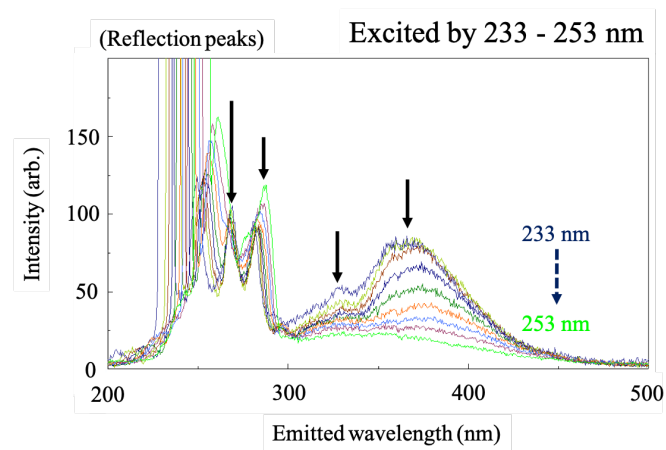
Figure 2.13: Fluorescence spectra of aerogel excited by UV lights. Four peaks were observed.
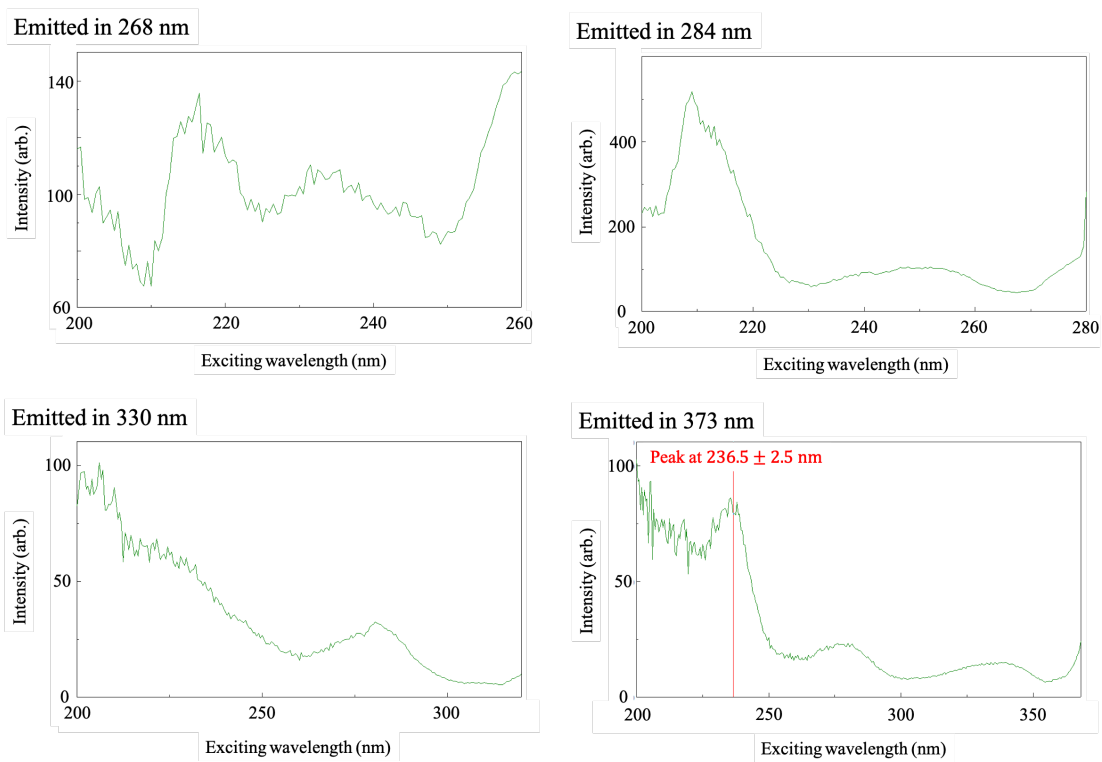
Figure 2.14: Intensities of fluorescent peaks versus excitation wavelength. No peak was observed at the wavelength of Ps Lyman-α (243 nm).

Table 2.4: Measured specification of the OPO laser.

Pulse energy	1 mJ
Pulse time duration	2 ns–5 ns
Line width (FWHM)	0.021 nm, 1.1×10^2 GHz
Beam diameter	6 mm
Repetition	10 Hz
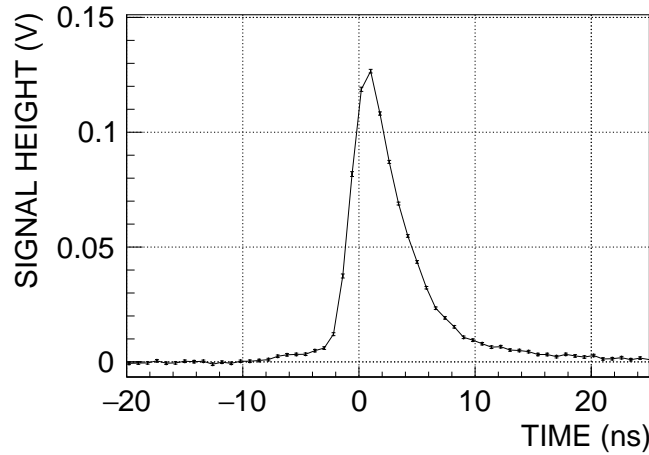
Figure 2.15: Time profile of the UV laser. The time duration of the laser pulse was assumed to be in 2 ns–5 ns by including a rise time of a digitizer.

2.3 Laser system

2.3.1 Hardware and specification

A wavelength tunable laser (Continuum, Panther EX OPO) was used to induce the Lyman-α transition of Ps. The OPO laser was pumped by a pulse Nd:YAG laser (Continuum, Surelite I-10). Specification of the OPO laser was measured and is summarized in Table 2.4. The output wavelength was calibrated with accuracy of 0.03 nm by a wavemeter (Coherent, WaveMate Deluxe). The pulse energy was measured by a thermal power meter (Ophir, 2A-BB-9).

A time profile of the pulse was measured by a fast photo detector (THORLABS, DET025A/M). Figure 2.15 shows an output waveform by the detector. The time duration of the laser pulse was assumed to be in 2 ns–5 ns by including a rise time of a digitizer (1.4 ns) described in section 2.5. This was a reasonable duration for the adopted OPO laser.

The line width was estimated by a transmittance spectrum through a solid Fabry-Pérot etalon. Table 2.5 summarizes specification of the custom-made etalon fabricated by SIGMAKOKI, and Figure 2.16 shows the transmittance spectrum. A spectrum profile of the laser was assumed to be Gaussian, and a convolved spectrum with the transmittance of the etalon was fitted to the measured

24

Table 2.5: Specification of the solid Fabry-Pérot etalon to measure the line width of the UV laser.

Base material	Synthetic silica glass
Thickness	330 µm
Reflectance per surface	98 %
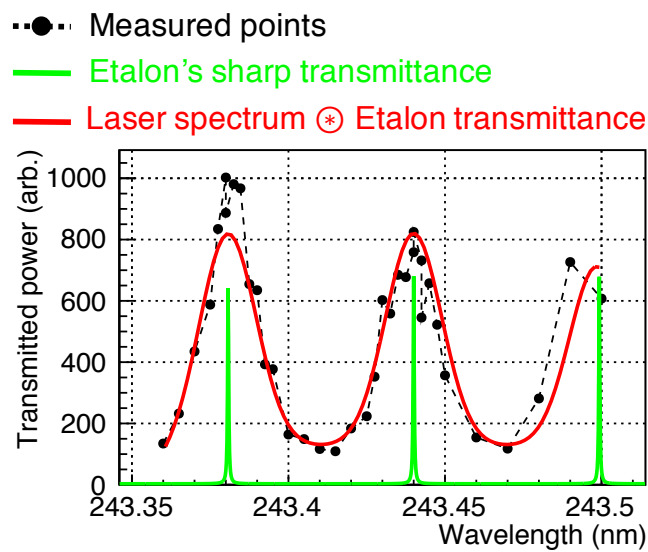
Figure 2.16: Transmittance spectrum through the solid etalon for line width measurement. The line width of the OPO laser was estimated to be 0.021 nm in FWHM.
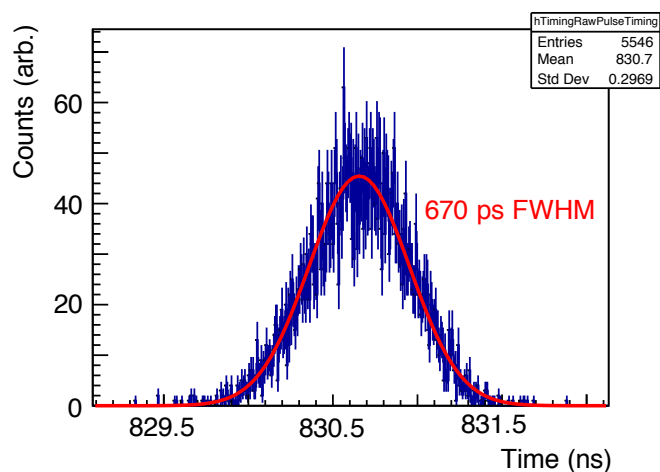
Figure 2.17: Timing differences between the trigger of the positron beam and the output of the OPO laser. The jitter was 670 ps in FWHM.

points. The transmittance spectrum of the etalon was estimated by the specification. The line width was estimated as 0.021 nm in FWHM. The corresponding bandwidth was 1.1×10^2 GHz. The width was reasonable for the OPO laser, and narrow enough to measure the expected resonance width of the transitions.

The OPO laser was synchronized with the positron beam. Timing of the irradiation was tunable with less than 1 ns jitter by a delay generator (Stanford Research Systems, DG535). Figure 2.17 shows a measured profile of timing differences between the trigger of the positron beam and the output of the OPO laser. The jitter was much smaller compared with the time duration of the pulse.

532 nm pulse lasers were also able to be irradiated to confirm the Lyman-α transition. 532 nm green lasers photoionize only 2P-Ps, which does not decay into annihilation γ-rays without affected by the material. 2P-Ps is dissociated into a positron and an electron, and then the annihilation of the positron becomes the signal of the transition. 1S-Ps is not photoionized because energy of a 532 nm photon is lower than the binding energy of 6.8 eV. The Surelite laser or another Nd:YAG laser (Spectra-Physics, GCR-250, 25 Hz repetition) were used as the photoionization laser. Either laser was able to output 1 mJ–10 mJ pulses with the similar time duration and beam size as the OPO laser. Figure 2.18 shows estimated photoionization rates and probabilities per a pulse for both wavelengths [48]. 532 nm lasers were powerful enough while photoionizations by 243 nm laser were negligible.

2.3.2 Path of lasers

The lasers were irradiated in two ways to perform types of the laser excitations. In one of which, the laser was irradiated on the aerogels in the counter propagating direction to the positron beam as shown in Figure 2.2. The confined Ps in the aerogel was mainly excited by this configuration. In the other way, the laser was irradiated at several millimeters away from the surface of the

26
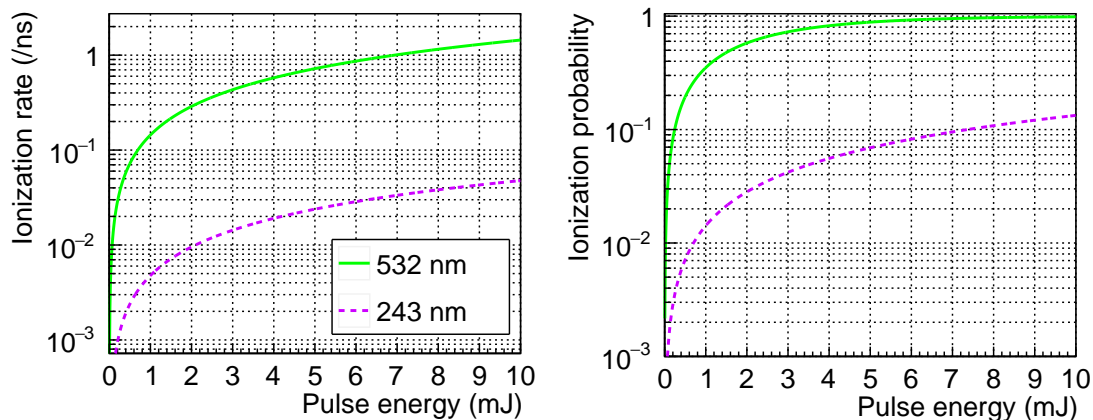
Figure 2.18: Photoionization rates and probabilities per a pulse by lasers. 532 nm lasers were powerful enough and photoionizations by 243 nm laser were negligible.

uncapped aerogel by being reflected at mirrors put in the chamber. Figure 2.19 show drawings of the modified chamber to allow the irradiation in this way. This configuration was adopted to excite Ps emitted in the outer vacuum of the aerogel. A demonstration of the Lyman-α transition in vacuum is useful to confirm whether the designed scheme works well and 2P-Ps behaves as expected without the material effects.

The components inside the chamber were modified to enable efficient excitations of Ps in vacuum. The sample holder was moved around 60 mm to downstream, and a multiple reflector was installed ahead the holder. Figure 2.20 show a magnified view around the multiple reflector and a detail description of the reflector. The lasers are reflected by mirrors (98 % reflectivity for both UV and green) more than 20 times to fill the space of around 50 mm, which is a typical distance that Ps travels, along the positron beam axis. Ps is also confined in the vertical direction to the lasers by silica wafers. Figure 2.21 shows an aligned path of the lasers. The picture was taken from the side of the γ-ray detector. A weak green laser for the alignment was irradiated. Multiple spots were observed at the mirror as the result of the multiple reflections. The UV laser and the ionizing green laser were expanded into around 10 mm diameter outside the chamber to increase the overlap with Ps. Ps can be always irradiated by the lasers while travelling in vacuum.

When the UV and the green laser are irradiated on this path, the intensity of annihilation γ-rays detected in a largely delayed region increases because the dissociated positron by the ionization is very slow to hit the surrounding materials. The typical distance to the surroundings was 50 mm in the configuration to excite Ps in vacuum.

2.4 Gamma-ray detector

LaBr$_3$(Ce) scintillator (1.5 inch diameter, 2 inch length) was selected as the γ-ray detector because LaBr$_3$(Ce) had a short decay constant of scintillation lights and good energy resolution. The former merit enabled to discriminate signals from prompt decays and o-Ps decays, and the latter to determine the decay mode of 2P-Ps in the material. The scintillator was coupled to

To be shown with magnified

Laser

Gamma-ray detector

10 cm

10 cm
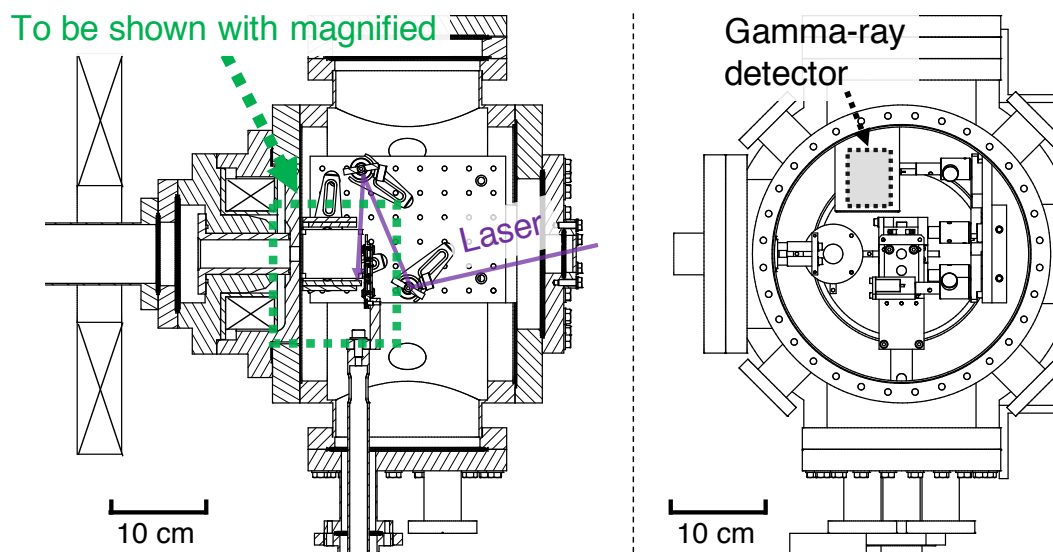
Figure 2.19: Drawings of the setup to excite Ps in vacuum. (Left) Cross sectional drawing of the chamber. The lasers were reflected by two mirrors inside the chamber to be irradiated ahead of the sample. Figure 2.20 shows magnified view around the sample. (Right) Drawing inside the chamber viewed from the downstream.

Ps & laser reflector

Laser

Uncapped aerogel

Silica mirrors to reflect lasers

Silica glass wafers to reflect Ps

55 mm
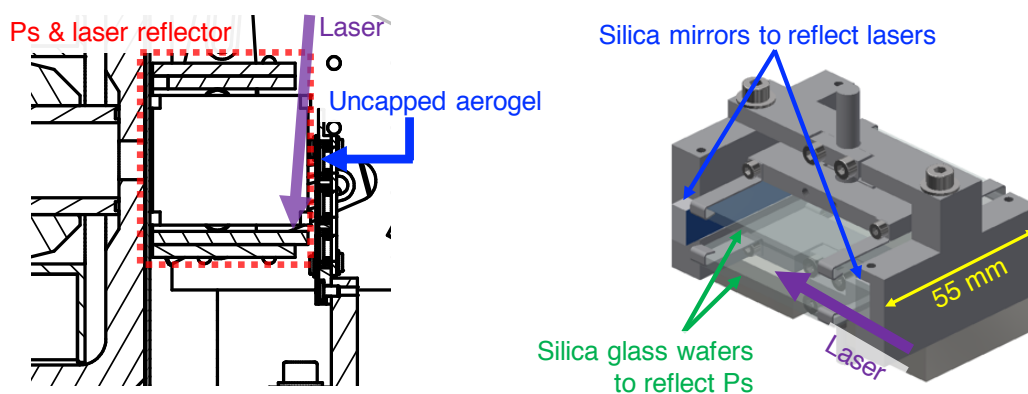
Laser

Figure 2.20: Multiple reflector for efficient excitation of Ps travelling in vacuum. (Left) Magnified view around the sample. (Right) Description of the multiple reflector. The lasers are reflected more than 20 times to fill the space of around 50 mm, which is a typical distance that Ps travels. Ps is confined in the vertical direction to the lasers by silica wafers.

28
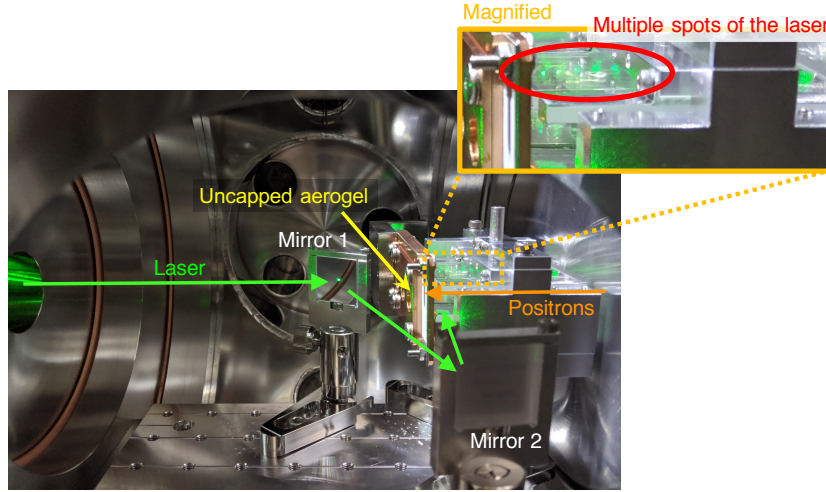
Figure 2.21: Path of the lasers to excite Ps in vacuum. Multiple spots were observed at a mirror as the result of the multiple reflections.

a HAMAMATSU R9869 photo multiplier tube (PMT). Figure 2.22 shows an averaged PMT output waveform by detecting 511 keV annihilation γ-rays from the Na-22 radioisotope. The waveform had the fast decay time constant of around 20 ns. Small dips appearing at around 65 ns were generated by a reflection of the electric signal. The waveform was regarded as a response of the detector. The response function was used in analysis as described in chapter 3. A function to reproduce the waveform [49] is modeled as

$$R(t) = \sum_{k=0}^{2} V_k \exp\left(-\frac{(\log((t - t_k)/\tau))^2}{2\sigma_k^2}\right).$$
(2.1)

The components with $k \geq 1$ represent the reflected signals. The parameters were determined by fitting to the waveform and summarized in Table 2.6. The reproduced function was superimposed in Figure 2.22.

Energy resolution of the detector was evaluated by detecting γ-rays from Na-22. Figure 2.23 shows the energy spectrum and the estimated resolution. Deposited energy was estimated by integrating waveforms. The energy dependent resolution was determined from resolutions of the pedestal and the two total absorption peaks to which Gaussian functions were fitted. High enough resolution was obtained to clearly observe the valley of Compton free region (340 keV–511 keV) of 511 keV γ-rays. This performance was essential to discriminate decay modes of Ps between 2γ and 3γ modes.

Timing resolution of the detector was estimated by detecting both of the two 511 keV annihilation γ-rays of positrons from the beta decay of Na-22. Each γ-ray was detected by the adopted γ-ray detector and a replicated one with the same type of the scintillator and the PMT. Figure 2.24 shows a spectrum of timing deference between total absorption signals of each detector. Arrival timings of signals were estimated by that when passing a certain threshold level. The resolution was estimated by fitting a Gaussian function to the spectrum and assuming both of the detectors
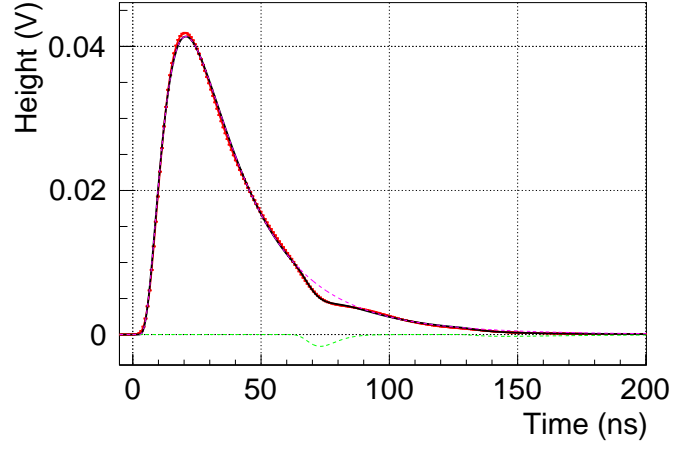
Figure 2.22: Response waveform of the γ-ray detector. Only total absorption events of 511 keV annihilation γ-rays were selected to generate the waveform. The response function which was used in the analysis is superimposed.

Table 2.6: Parameters to reproduce the response waveform of the γ-ray detector.

τ	19.2 ns
V_0	0.0414 V
t_0	1.43 ns
σ_0	0.688 ns
V_1	$-0.0396V_0$
t_1	52.4 ns
σ_1	0.279 ns
V_2	$-0.00598V_0$
t_2	125 ns
σ_2	0.851 ns
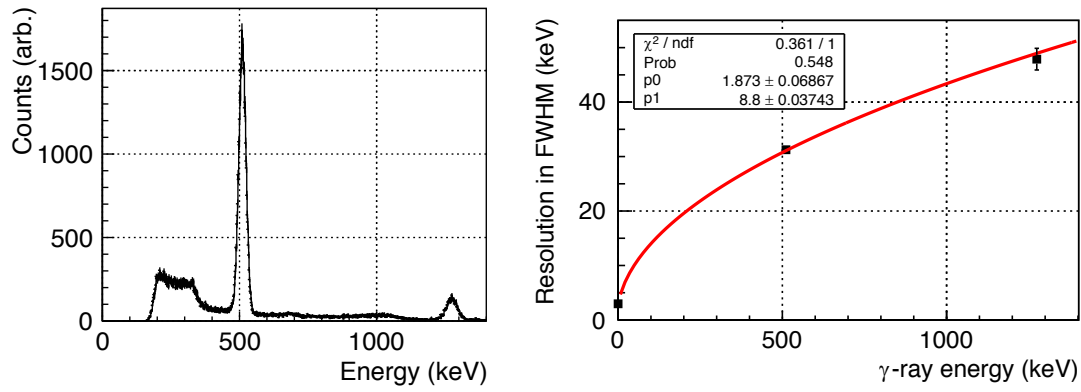
Figure 2.23: (Left) Energy spectrum by detecting γ-rays from Na-22. (Right) Estimated energy resolution. The function of $\sigma = \sqrt{p_0 E + p1}$ was fitted to estimate the energy dependent resolution.
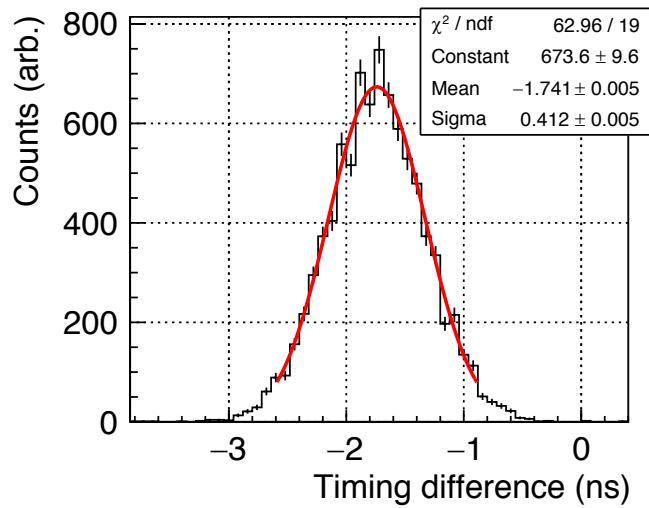
Figure 2.24: Timing difference spectrum of the two detectors. A high enough resolution of 680 ps in FWHM was achieved.
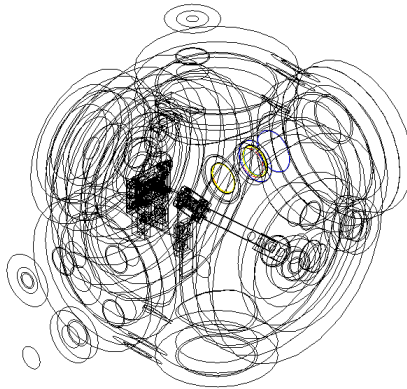
Figure 2.25: Input geometry in the Geant4 Monte Carlo simulation.

contributed in the same weight for the observed jitter. High enough resolution of 680 ps in FWHM was achieved to measure the anticipated timing structure of γ-rays from decays of 2P-Ps.

2.5 Data acquisition system

Output waveforms of the γ-ray detectors and the photo detectors for lasers were recorded by a digitizer (National Instruments, PXIe-5162). High impedance terminals were used to record large signals from γ-ray detector. A sampling rate was 1.25 GHz and a bandwidth 300 MHz for the configuration. The signal from the γ-ray detector was recorded by two channels with different scales to record waveforms in a wide dynamic range with small quantization noises. The photo detectors were prepared for both of the UV laser and the green laser, and used to select data with or without each laser irradiation. Data acquisitions (DAQ) were triggered by logic trigger signals from the positron beams of 50 Hz. A typical DAQ rate was 47 Hz as 94 % of the triggers.

2.6 Monte Carlo simulation

A Monte Carlo simulation was performed to estimate detection efficiencies of the γ-rays and energy deposition spectra for each decay mode of Ps. Figure 2.25 shows a geometry input in the Geant4 Monte Carlo simulator. Figure 2.26 shows obtained energy deposition spectra by each mode of the decay. Mean deposition energies and total detection efficiencies are summarized in Table 2.7.
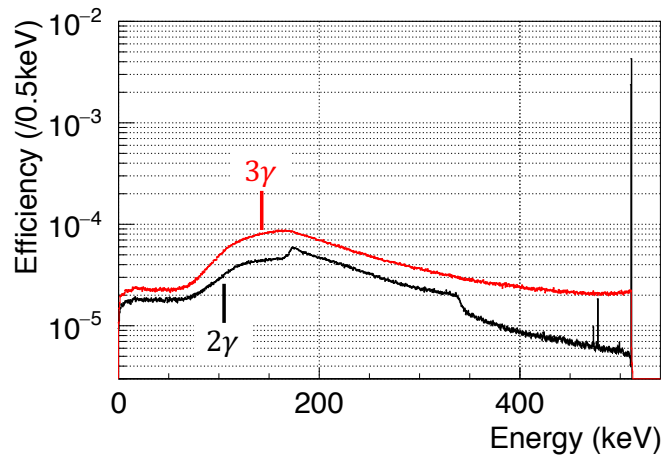
Figure 2.26: Energy spectra of each decay mode by Monte Carlo simulation.

Table 2.7: Simulated detection efficiencies and mean deposition energies.

Decay mode	Mean deposition	Total efficiency
3γ	226 keV	4.11 %
2γ	272 keV	3.07 %

Chapter 3

Analysis Methods

This chapter describes analysis methods to measure decay rates of Ps. The decay rates were estimated by data suffering from many pileups of annihilation γ-rays by the bunched positrons. Typical output waveforms of the PMT are shown in Figure 3.1 by the full range, and in Figure 3.2 by the enlarged range. More than ten γ-rays were detected from the prompt decays, and the majority of the delayed signals from o-Ps decays were piled up on others. Two methods were adopted to be applied for the waveforms with such pileups. One analyzes averaged waveforms of the PMT output. This method is called Single-Shot Positron Annihilation Lifetime Spectroscopy (SSPALS) [50], which is expected to be robust for the pileups but yield only averaged information. The other simply analyzes each single waveform to measure timings and heights of each γ-ray's signal. A high-pass filter was applied on waveforms to reduce the pileup effects in this pulse-by-pulse analysis. This method can yield energy and timing spectra of each annihilation event while the applicable range is limited in a delayed region with less pileups. Procedures of the methods are explained and validated through applications on data results of which were expected. A phenomenological model to calculate intensities of annihilation γ-rays from applied laser field and the decay rate of 2P-Ps is also introduced. The decay rate of 2P-Ps is quantitatively estimated by comparing predictions by the model with measured data.

3.1   Method based on an averaged waveform (SSPALS)

In the SSPALS method, waveforms are averaged over bunches of the positron beam, and then the averaged waveform is used as the target of the fitting. An expected waveform is generated by convolving an assumed signal function with the response waveform of the γ-ray detector shown in Figure 2.22. A sum of squared residuals of each point, which are weighted by inverses of variances of each point, is minimized to estimate parameters in the assumed signal function. The Monte Carlo method is adopted in this work to estimate statistical uncertainties and p-value assuming Poisson distributions for detected numbers of events to take into account the correlation between each point in the waveform.
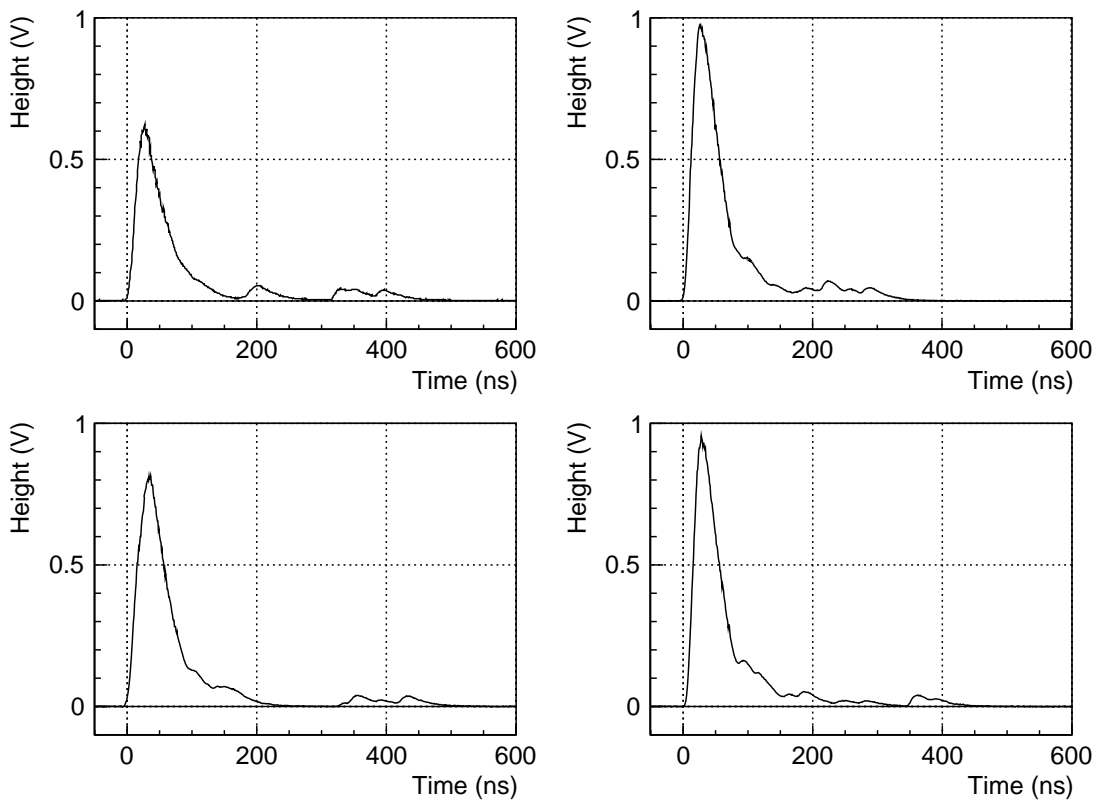
Figure 3.1: Typical waveforms of the output of the PMT in the full range. More than ten γ-rays were detected from the prompt decays.
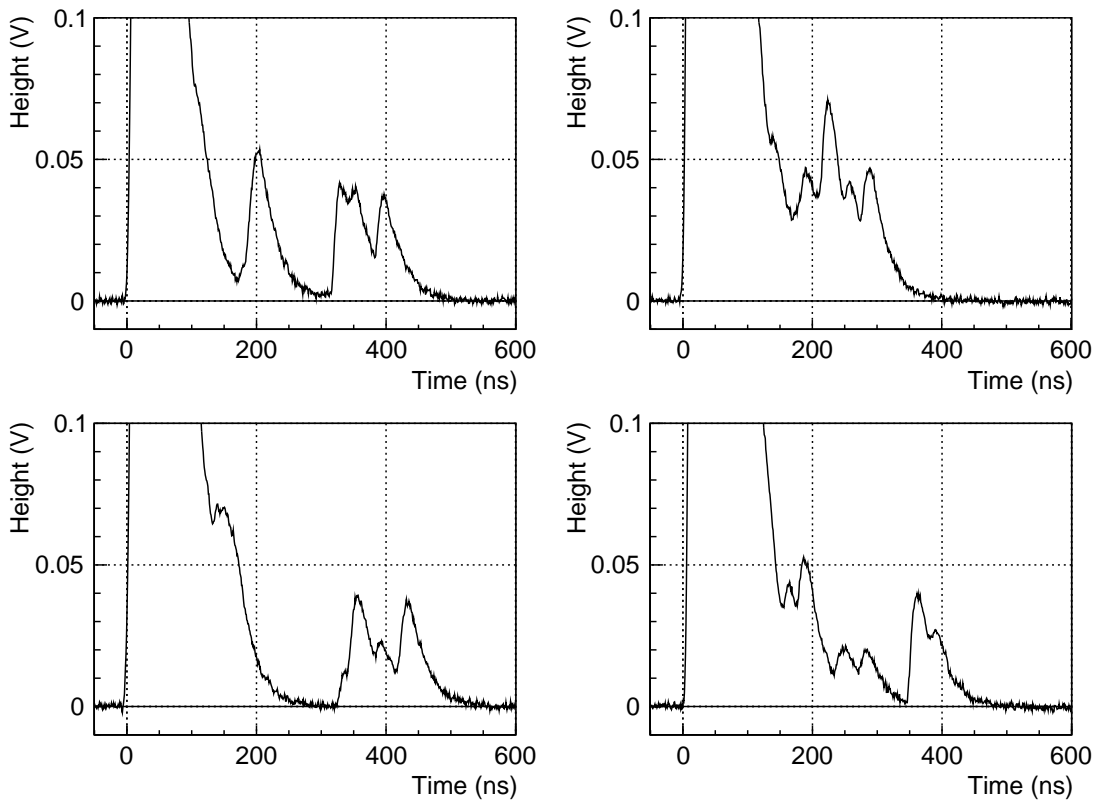
Figure 3.2: Typical waveforms of the output of the PMT in the enlarged range. The majority of the signals were piled up on others.

37

3.2 Pulse-by-pulse analysis method

Energy depositions and timings of each detected γ-ray can be acquired by applying peak detections on each single waveform. This method is valid in a later timing region from the positron irradiation where less annihilation γ-rays are piled up.

A high-pass filter was applied to waveforms in offline to reduce the timing width of each pulse and then to ease the distortion effects by pileups. A simplified Wiener filter was chosen. A characteristic function of the filter, $H(\omega)$, is formulated in Fourier space as

$$H(\omega) = \frac{R(\omega)^*}{|R(\omega)|^2 + |R(\omega_c)|^2},$$ (3.1)

where $R(\omega)$ is Fourier transformation of the response function (Equation 2.1). ω_c is a cut-off angular frequency to suppress high frequency noises. ω_c was determined to be 0.33 GHz to retain the same level of signal-to-noise ratios as original waveforms. Figure 3.3 shows the adopted characteristic function. The function was scaled so that signal amplitudes were not changed.

Performances of the filter were evaluated by data detecting γ-rays from Na-22. Figure 3.4 show comparisons of raw and filtered waveforms with various amplitudes. The time durations of the pulses were narrowed to around 10 ns by the filter. Timings and heights of the peak points were regarded as detected timings and energy depositions of γ-rays with setting an appropriate threshold.

Linearity and energy resolution were checked by comparing with values yielded from analyzing raw waveforms. Figure 3.5 show a correlation of estimated energy depositions and energy spectra by Na-22. Peak heights of filtered pulses were proportional to energy depositions which were evaluated by integrating raw waveforms. The energy resolution shown in Figure 3.6 was still good enough to clearly observe the valley of Compton free region (340 keV–511 keV) of 511 keV γ-rays. This good resolution would enable to discriminate decay modes of Ps between the 2γ and 3γ modes.

A timing resolution was evaluated in the same way as section 2.4. Figure 3.7 shows timing spectra of the peaks. The good timing resolution of 640 ps in FWHM was achieved with a tiny time walk effect over 150 keV. The resolution of the reference detector (680 ps FWHM) was subtracted to evaluate the contribution from the single detector.

3.3 Quality check of analysis

Analyses were applied on data acquired by using the bunched positrons to check qualities of the methods. All of the data analyzed here were acquired without irradiating any lasers. The two analysis methods were confirmed to yield the expected decay rates and production probabilities of 1S-Ps, and energy distributions of annihilation γ-rays from 1S-Ps decays. In this section, statistical uncertainties are quoted on estimated parameters.

38
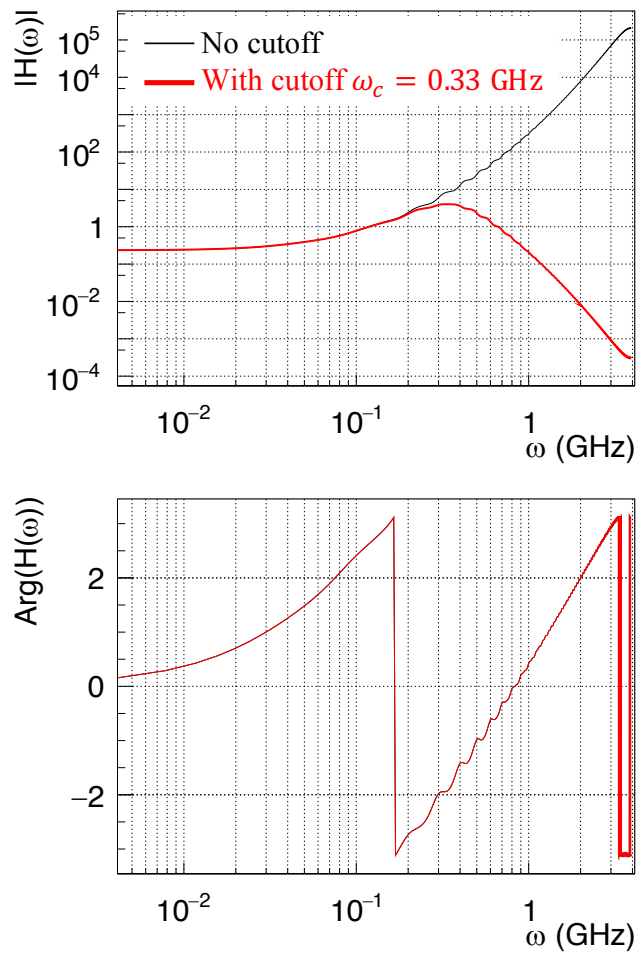
Figure 3.3: Magnitude (top) and argument (bottom) of the characteristic function of the high-pass filter

39
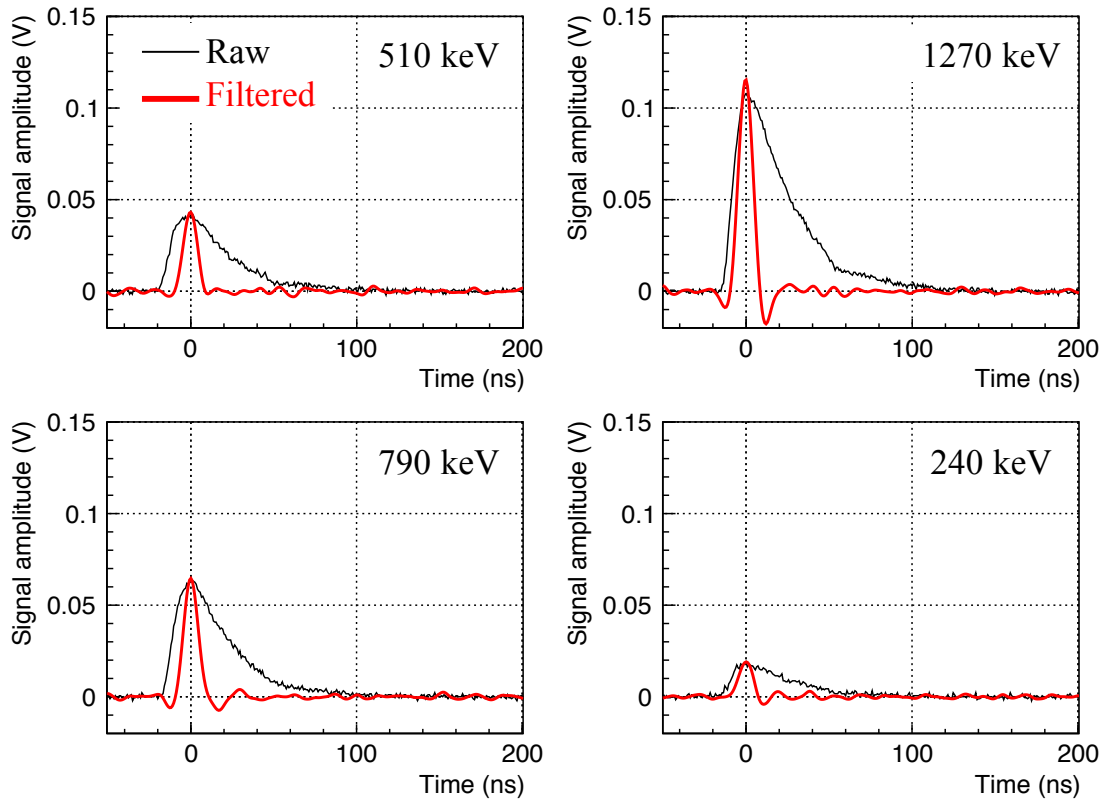
Figure 3.4: Comparison of raw and filtered waveforms. The time durations of the pulses were narrowed by the filter from 30 ns to 10 ns in FWHM.
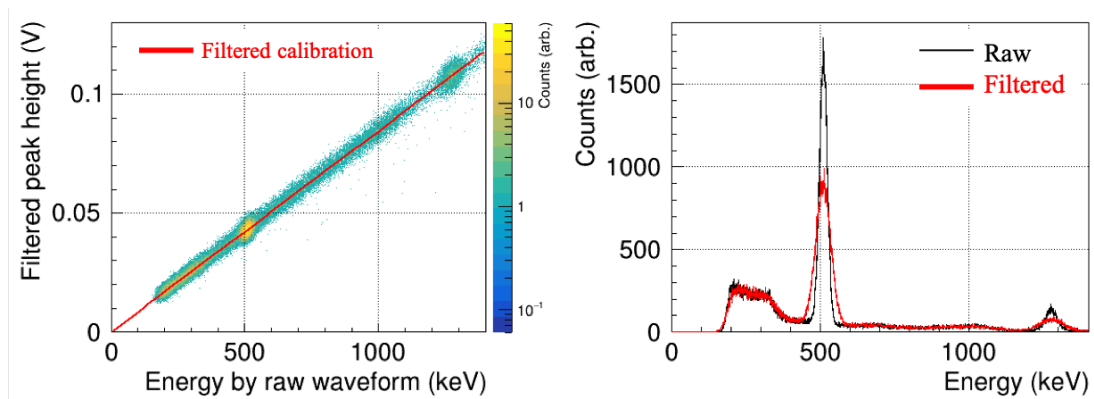
Figure 3.5: (Left) Correlation between filtered pulse peak heights and energy deposition estimated by integrating raw waveforms. (Right) Energy spectra. Good enough linearity and resolution were achieved.
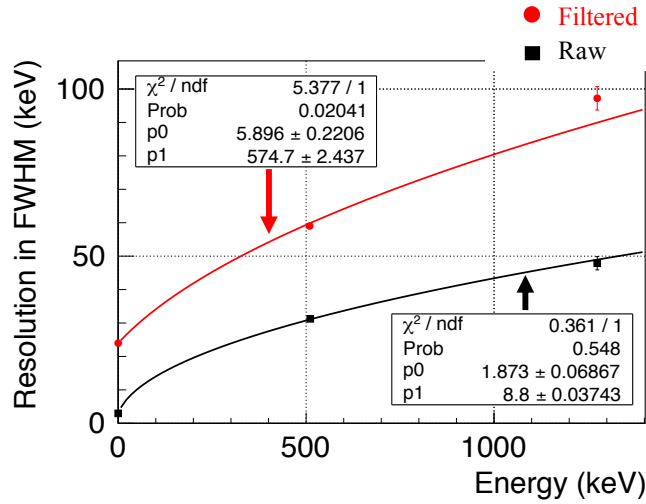
Figure 3.6: Energy resolution of filtered waveform analysis. The fitted functions were $\sqrt{p0 \times \text{Energy} + p1}$. The resolution is good enough to discriminate a decay mode of Ps.
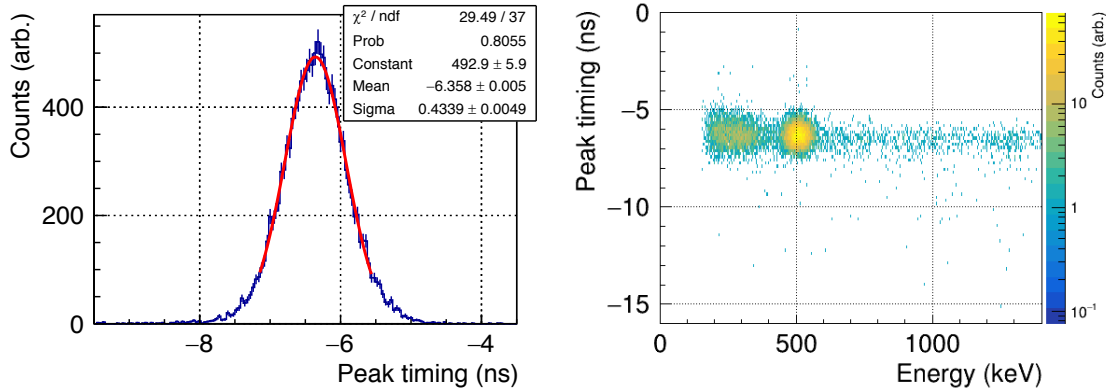
Figure 3.7: (Left) Timing spectrum of the filtered pulses' peak. (Right) Correlation between heights and timings. The timing resolution was as good as that evaluated by the raw waveforms.

3.3.1 Decay rate and production probability

Application of the Ps decay model

Time dependent intensity of annihilation γ-rays, $S(t)$, is modeled to deduce decay rates and production probabilities of o-Ps in 1S state. The model was formulated as

$$S(t) = \varepsilon_2 N_{prompt}\delta(t) + (\varepsilon_2\Gamma_{po}(t) + \varepsilon_3\Gamma_s)N_{oPs}\exp\left(-\int_0^t (\Gamma_{po}(t') + \Gamma_s)\mathrm{d}t'\right). \qquad (3.2)$$

The first term represents the prompt decay of p-Ps or positrons which do not form Ps. Those components generate annihilation γ-rays in less than 1 ns, which is considered to have the delta functional spectrum for the measurement system in the present work. The second term represents the signal from decays of o-Ps. As for meanings of the symbols, ε_n are detection efficiencies of $n\gamma$ decay. Γ_s and Γ_{po} are decay rates of the self decay and the pick-off decay of o-Ps respectively. Γ_{po} may depend on time by the thermalization process. N_{prompt} and N_{oPs} are produced numbers of each component. The production probability can be calculated as $\frac{4}{3}N_{oPs}/(N_{oPs} + N_{prompt})$ considering the spin statics. The detection efficiencies are multiplied by the simulated mean energy depositions when combined with the SSPALS analysis.

In the SSPALS analysis, the time profile of the positron beam was treated in different ways to be combined with the decay model. For the prompt decay component, the waveform acquired with the kapton target was used without being convolved with the response function, because the prompt decay was the dominant component in the kapton target. N_{prompt} and a timing of the pulse were set to be free parameters in the fitting. For the o-Ps component, a time profile of the positron beam was assumed, and then was convolved with the model function. The timing profile was assumed to be a convolution of the beam timing profile in short time duration (Figure 2.3) and a Gaussian function which could have different widths for both sides. The Gaussian function was used for modeling a timing jitter of the positron beam during data acquisition duration, which was typically ten minutes. The widths were determined to reproduce the waveform acquired with the kapton target by convolving the beam timing profile and the response of the detector. Figure 3.8 shows the assumed timing profile, and compares the kapton waveform with the reproduced one. The origin of the timing was determined so that the waveform with the kapton started from the origin. One sigma widths of the jitter function were determined to be 1.0 ns in negative and 13.7 ns in positive. The convolved timing profile was used hereafter in the SSPALS analysis. A systematic uncertainty from this assumption is estimated by adopting wider and narrower profiles. The wider profile was determined to include the whole kapton waveform. The short time duration profile was used as the narrower profile.

Applying SSPALS analysis

The SSPALS analysis was applied on data using silica aerogels as targets and the parameters was confirmed to be consistent with other measurements described in section 2.2. Figure 3.9 shows results of fitting the reproduced waveform to a measured waveform by the capped aerogel. The waveform was reproduced well by the SSPALS analysis. The production probability was estimated as 26.9 ± 0.6(stat.) %, which reasonably agreed with the other measurement described
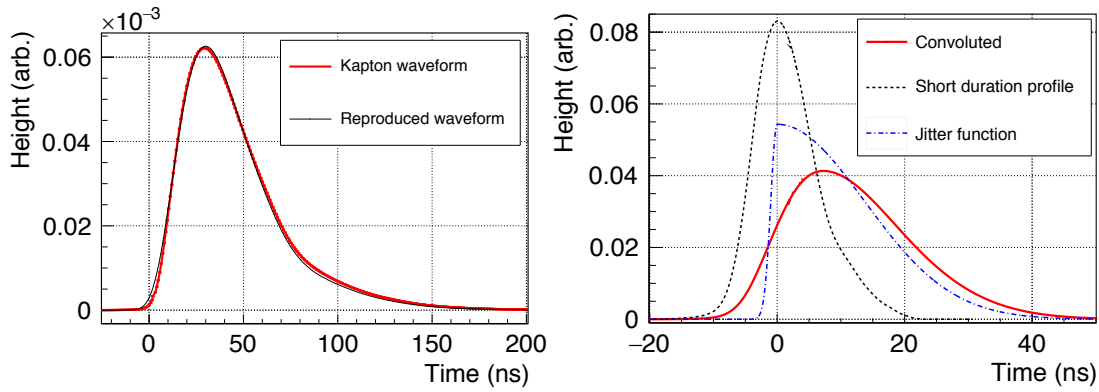
Figure 3.8: (Left) Comparison between the kapton and reproduced waveform. (Right) Assumed timing profile of positron beam. One sigma widths of the jitter function were $1.0\,\text{ns}$ in negative and $13.7\,\text{ns}$ in positive.
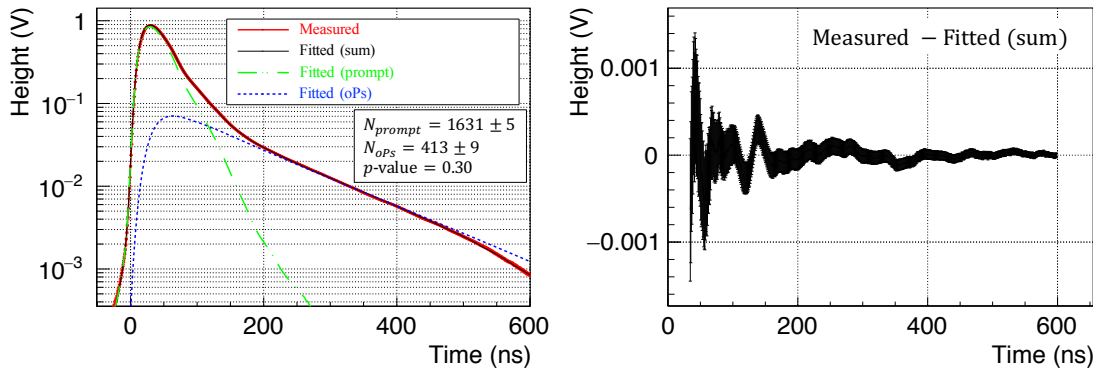
Figure 3.9: (Left) Measured and fitted waveforms. The fitted waveforms and intensities of each component in the decay model are superimposed. (Right) Residuals of the fit.
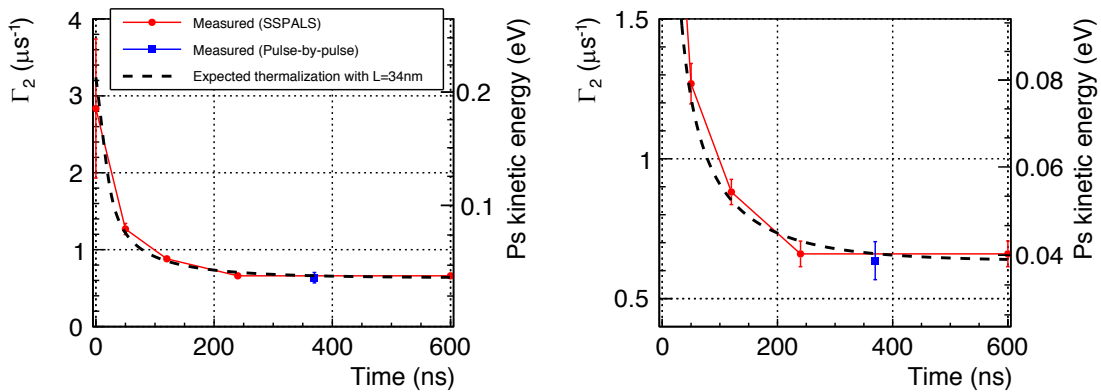
Figure 3.10: Pick-off decay rates in the capped aerogel by the SSPALS analysis. The expected evolutions by the thermalization process described in section 1.1.2, and a result from the pulse-by-pulse analysis are superimposed. The right figure is the enlarged view of the left.
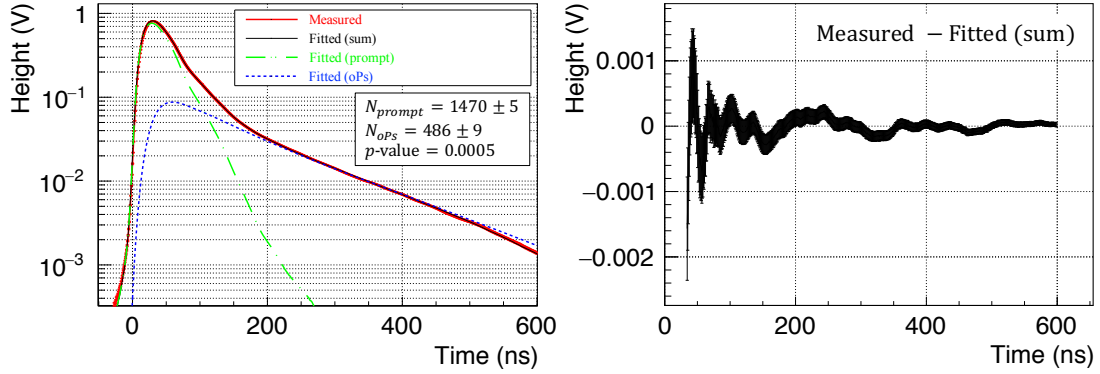
Figure 3.11: (Left) Measured and fitted waveforms. The fitted waveforms and intensities of each component in the decay model are superimposed. (Right) Residuals of the fit.
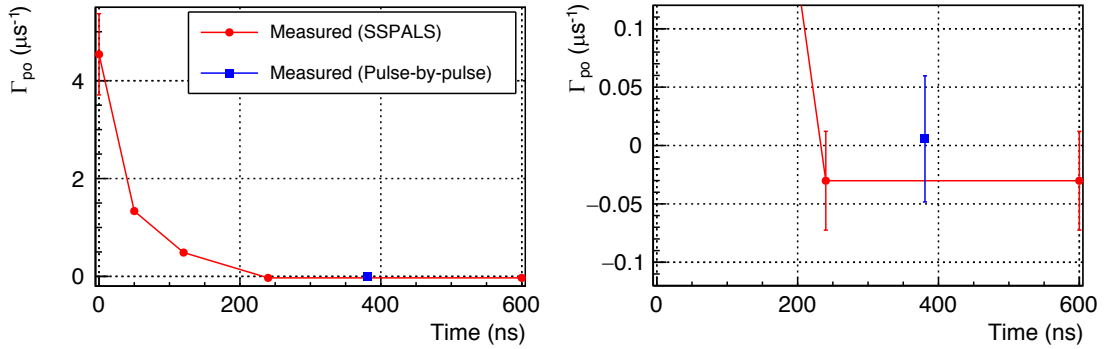
Figure 3.12: Pick-off decay rates in the uncapped aerogel by the SSPALS analysis. A result from the pulse-by-pulse analysis is superimposed. The right figure is the enlarged view of the left.

in section 2.2. The estimated pick-off decay rates were shown in Figure 3.10. The timing region was divided into four parts (0 ns–50 ns, 50 ns–120 ns, 120 ns–240 ns, and 240 ns–600 ns), and the pick-off rates at each start time of the regions were set to be free parameters. The rates inside each time region but the last one were assumed to be linear functions. In the last region, the rate was set to be constant. The rates after 50 ns were consistent with the expected function by the thermalization process described in section 1.1.2. The mean free path to draw the expected function was estimated to be 34 nm to reproduce the thermalized pick-off decay rate. When estimating the thermalization process, kinetic energy of Ps was averaged over the timing profile of the positrons. In the first time region, the result would not be so reliable and mainly determined by the linear constraint from the second region because a systematic error should be large due to the large amplitude from prompt decays. The N_{oPs} and the first decay rate were strongly correlated each other.

The results for the uncapped aerogel were shown in Figure 3.11 and Figure 3.12. The higher production probability as $33.0 \pm 0.6(\text{stat.})\%$ was obtained without the cap because more positrons stopped in the pore network of the aerogel. The pick-off rate at well thermalized

44
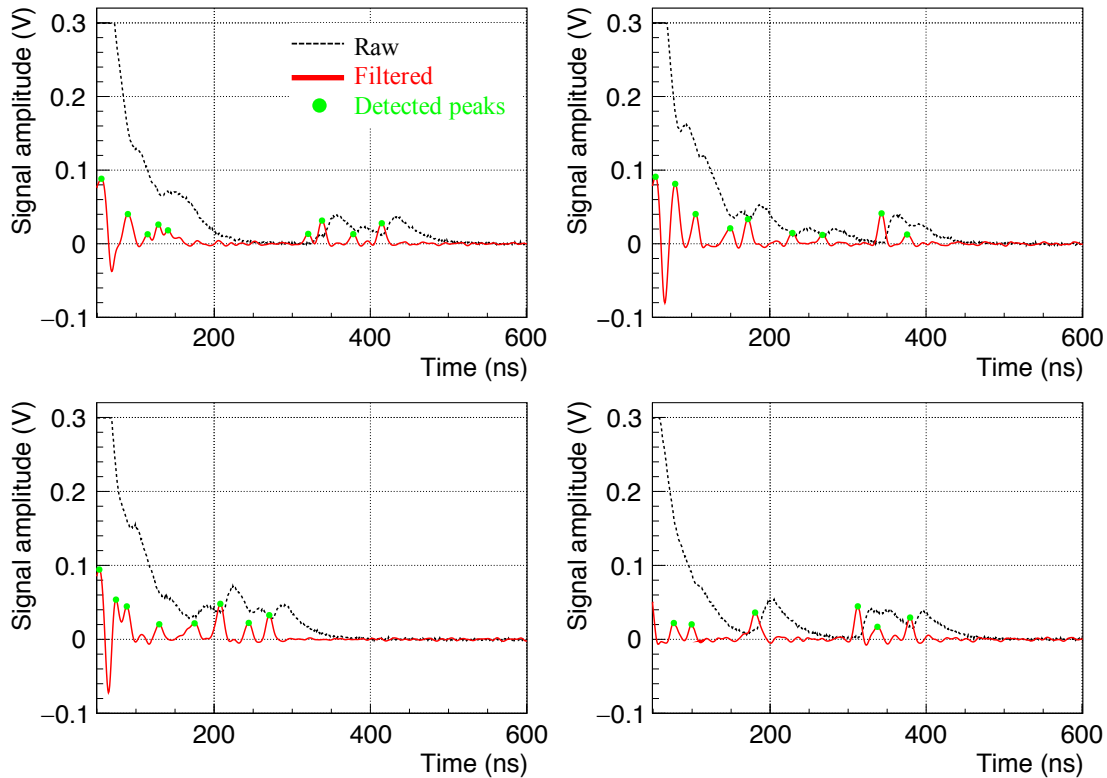
Figure 3.13: Filtered waveforms and detected peaks in the pulse-by-pulse analysis. A lot of pileups were removed and the simple process to detect peaks was valid.

timing was consistent with zero as expected from the observation that o-Ps escaped into the outer vacuum of the pores without the cap. In conclusion, the SSPALS analysis was able to quantitatively measure properties of o-Ps in most of the timing regions.

Applying pulse-by-pulse analysis

The pulse-by-pulse analysis was also applied to the same data. Typical waveforms on which the high-pass filter was applied, and detected peaks are shown in Figure 3.13. Waveforms recorded in the enlarged range were used in the pulse-by-pulse analysis to avoid large quantization noises. A lot of pileups were removed after around 200 ns where the tails of the large signal from the prompt decays became small. The simple process to detect peaks was valid for the filtered waveforms.

The thermalized pick-off rates were estimated by fitting the o-Ps decay model to timing spectra shown in Figure 3.14. Pulses with more than 240 keV energy deposition were included in the spectra to reject fake peaks by noises or ringing side peaks. The rates were assumed to be constant in the fitting region (240 ns–1200 ns), and are shown in Figure 3.10 for the capped and Figure 3.12 for the uncapped. Both results were consistent with those from the SSPALS analysis.

45
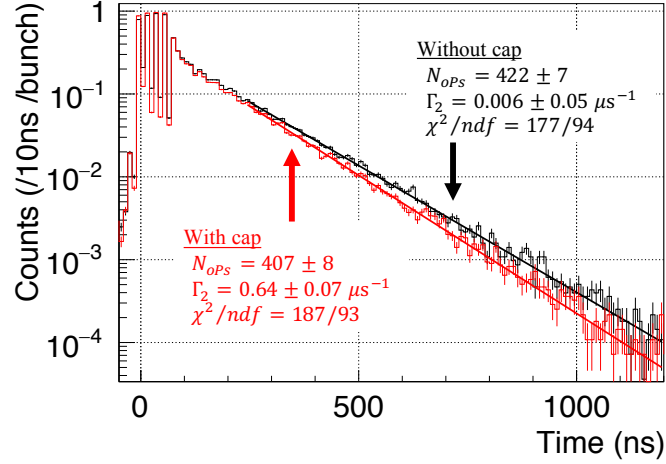
Figure 3.14: Timing spectra of o-Ps decays through the pulse-by-pulse analysis. The fitting yielded the consistent estimations with the SSPALS analysis as shown in Figure 3.10 and Figure 3.12.

N_{oPs} with the cap agreed between the both methods, but without the cap 15% less number was estimated in the pulse-by-pulse analysis compared with the SSPALS analysis. There would be systematic errors originating from an extrapolation of the model function to $t = 0$, which was an unavoidable procedure in this pulse-by-pulse analysis due to the large pileups at the prompt region. For example, annihilations in early timing, such as decays of very fast Ps hitting walls of the chamber, were not able to be detected in the pulse-by-pulse analysis to result in estimating the less number of Ps. Errors from the extrapolation would be evaluated when estimating the decay rate of 2P-Ps.

When estimating the uncertainty of the parameters, statistical uncertainties of each bin were scaled for the reduced chi-square to be unity. The poor goodness-of-fit would be attributed to residual pileup effects.

The gain by the high-pass filter can be confirmed by comparing the timing spectrum with that produced by simple processes to detect timings of rise-ups in the waveform without the filter. The timing spectra for the aerogel with the cap are compared in Figure 3.15. Both spectra agreed after around 600 ns where less pileups occurred, but less signals were detected without the filter in the earlier timing. A spuriously longer lifetime than that of o-Ps in vacuum was obtained by fitting the decay model to the spectrum which effectively had the less detection efficiency. The high-pass filter worked well to ease the pileup effects and obtain the physical and reasonable decay rate of Ps.

3.3.2 Energy of gamma-rays from Ps decay

An energy spectrum of γ-rays from Ps decay was produced through the pulse-by-pulse analysis and compared with the Monte Carlo simulation to validate the analysis method. Figure 3.16 shows the measured and simulated spectra for the aerogel with the cap. Pulses detected after
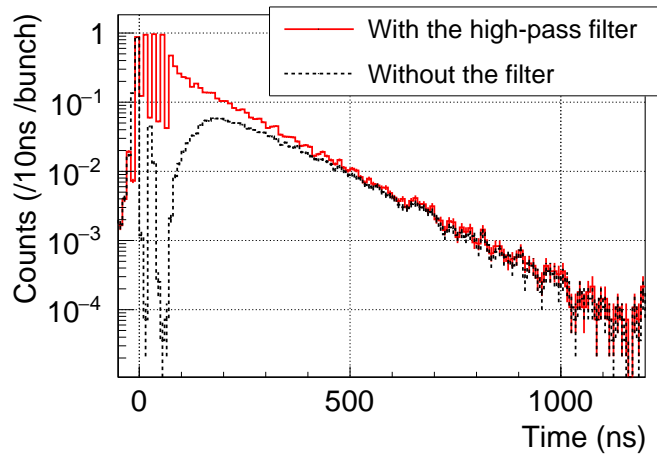
Figure 3.15: Comparison of timing spectra with and without the high-pass filter. Without the filter, less signals were detected in 200 ns–600 ns due to the pileups.
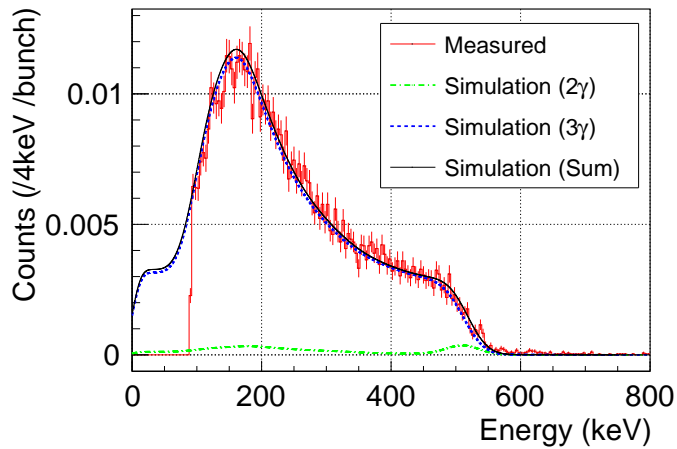
Figure 3.16: Energy spectrum of annihilation γ-rays from o-Ps by the pulse-by-pulse analysis. The spectrum reasonably agreed with the MC simulation, whose mean deposition energy was differed by only 2 % with the measurement. The pulse-by-pulse analysis had the good sensitivity to distinguish the decay modes of Ps. The deviation of the mean deposition energy is considered to be the magnitude of the systematic uncertainty.

47

400 ns were collected in the spectrum. The simulated 2γ and 3γ spectra were added according to branching ratios of each decay mode, which were determined by the thermalized pick-off rate, and then scaled. A good agreement between the measurement and the simulation was observed. The pulse-by-pulse analysis is expected to have good enough sensitivity to distinguish the decay modes of Ps.

A discrepancy of the mean deposited energies between the measurement and the simulation was 2 %. This value is used to evaluate the systematic uncertainty from the MC simulation.

3.4 Model of excitation and decay of 2P-Ps

3.4.1 Equations of internal states

A new formalization is introduced in order to quantitatively estimate the decay rate of 2P-Ps. The decay rate is included in the following optical Bloch equations [51], by which a density matrix of the Ps internal states under the irradiation of the UV laser evolves.

$$\frac{d}{dt}\rho_{11} = \frac{i}{2}\Omega(\rho_{12} - \rho_{21}) - \Gamma_1\rho_{11} + (\Gamma_{sp} + P_1\Gamma_2)\rho_{22}, \tag{3.3}$$

$$\frac{d}{dt}\rho_{12} = \frac{d}{dt}\rho_{21}^* = \frac{i}{2}\Omega(\rho_{11} - \rho_{22}) + \left(i(\omega_{21} - \omega_L) - \frac{1}{2}(\Gamma_1 + \Gamma_{sp} + \Gamma_2)\right)\rho_{12}, \tag{3.4}$$

$$\frac{d}{dt}\rho_{22} = -\frac{i}{2}\Omega(\rho_{12} - \rho_{21}) - (\Gamma_{sp} + \Gamma_2)\rho_{22}. \tag{3.5}$$

An intensity of annihilation γ-rays from the decay can be calculated by the density matrix. These equations are numerically solved with inputting parameters of the laser, and then the decay rate of 2P-Ps will be estimated by fitted to measured timing spectra of the annihilation γ-rays. Definitions of the symbols are as follows:

ρ_{ij}: Elements of the density matrix. $\rho_{ij} = c_i^* c_j$ where c_i is a probability amplitude of $n = i$ state.

ω_{21}: Resonant angular frequency of the Lyman-α transition.

Γ_1: Annihilation decay rate of the 1S state. This is the sum of the self decay rate and the pick-off decay rate of o-Ps.

Γ_{sp}: Spontaneous decay rate of the 2P state.

ω_L: Angular frequency of the irradiated laser.

Ω: Rabi frequency determined by electric field of the laser.

Γ_2: Decay rate of 2P-Ps in the material.

P_1: Branching ratio of a process in which a dissociated positron forms 1S-Ps.

Γ_2 is the target quantity to be estimated, and P_1 is also phenomenologically introduced to describe a possible process in the material. 2P-Ps is modeled to be dissociated into a positron and an electron with the rate of Γ_2. The dissociated positron would form 1S-Ps again with a probability of P_1, and the remained is assumed to decay into annihilation γ-rays. It would be possible to set a physical limit on P_1 from around 0.2 to 0.4, which is an assumed range of the o-Ps production probability inside the silica aerogel used in the present work. P_1 was assumed to be 0.3 according to measurements of production probabilities of o-Ps in the present work.

A total increase of the decay rate of Ps by the laser irradiation can be calculated by a following expression:

$$\Gamma_L(t) = \frac{\rho_{11}(t)\Gamma_1 + \rho_{22}(t)(1 - P_1)\Gamma_2}{\rho_{11}(t) + \rho_{22}(t)} - \Gamma_1. \tag{3.6}$$

Time dependent intensity from decays of Ps can be formulated by adding $\Gamma_L(t)$ to Equation 3.2 as

$$S(t) = \varepsilon_2 N_{prompt}\delta(t)$$
$$+ (\varepsilon_2 \Gamma_{po}(t) + \varepsilon_3 \Gamma_s + \varepsilon_L \Gamma_L(t))N_{oPs} \exp\left(-\int_0^t (\Gamma_{po}(t') + \Gamma_s + \Gamma_L(t'))dt'\right). \tag{3.7}$$

ε_L is the detection efficiency for γ-rays from the decays of 2P-Ps. The decay mode of 2P-Ps will be also inspected.

3.4.2 Predictions by the model

$\Gamma_L(t)$ can be calculated by inputting modeled laser fields. Rabi frequency Ω depends on the electric field of the laser, and Ω determines the excitation efficiency. Ω can be calculated as $\Omega(t) = e \langle 2P|r|1S\rangle E(t)/\hbar$, where $e \langle 2P|r|1S\rangle$ is a dipole moment evaluated in an overlap of the wave function of each state, and $E(t)$ is an envelope of the electric field of the laser. $E(t)$ was modeled by Fourier transform of a multi-mode Gaussian spectrum $\tilde{E}(\omega)$:

$$E(t) = \frac{E_0}{2\pi}\frac{\Delta_\omega}{\sigma_\omega}\vartheta_3\left(\frac{\Delta_\omega t}{2}, \exp\left(-\frac{\Delta_\omega^2}{2\sigma_\omega^2}\right)\right)\exp\left(-\frac{t^2}{2\sigma_t^2}\right), \tag{3.8}$$

$$\tilde{E}(\omega) = E_0 \sum_{k=-\infty}^{\infty} \Delta_\omega \frac{1}{\sqrt{2\pi}\sigma_\omega}\exp\left(-\frac{(k\Delta_\omega)^2}{2\sigma_\omega^2}\right)\frac{\sigma_t}{\sqrt{2\pi}}\exp\left(-\frac{(\omega - k\Delta_\omega)^2}{2(1/\sigma_t)^2}\right). \tag{3.9}$$

$\vartheta_3(z, \tau)$ is the elliptic theta function, E_0 amplitude of the field, σ_ω band width, σ_t time duration of pulse, and Δ_ω interval of the modes. Here $1/\sigma_t$ becomes a band width of each mode. σ_t and σ_ω were set to reproduce the timing profile and frequency spectrum of the UV laser. E_0 was determined according to the pulse energy and the beam diameter of the laser, and averaged over the spacial profile of the positrons. Δ_ω was assumed to be $2\pi\times1.0$ GHz by a length of the resonator in the OPO laser. Figure 3.17 show a calculated timing profile and a frequency spectrum using $\sigma_t = 3$ ns and $\sigma_\omega = 2\pi \times 64$ GHz. By squaring the field amplitude to get the power profile, it can be confirmed that the measured time duration of the pulse (5 ns) and band width (1.1×10^2 GHz) as described in subsection 2.3.1 were reproduced.

49
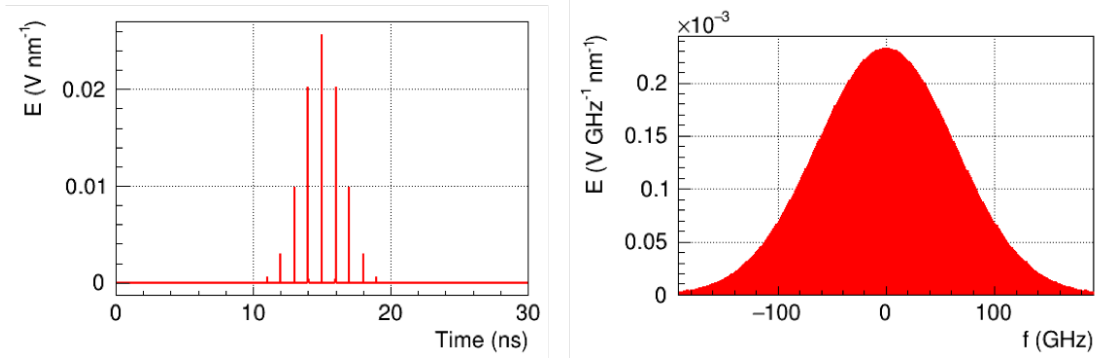
Figure 3.17: Simulated laser field. (Left) timing profile. (Right) Frequency spectrum. The power profile and spectrum can be obtained by squaring the field amplitudes to be compared with the measured pulse time duration and the band width.

(a) ρ_{11} element.

(b) ρ_{22} element.
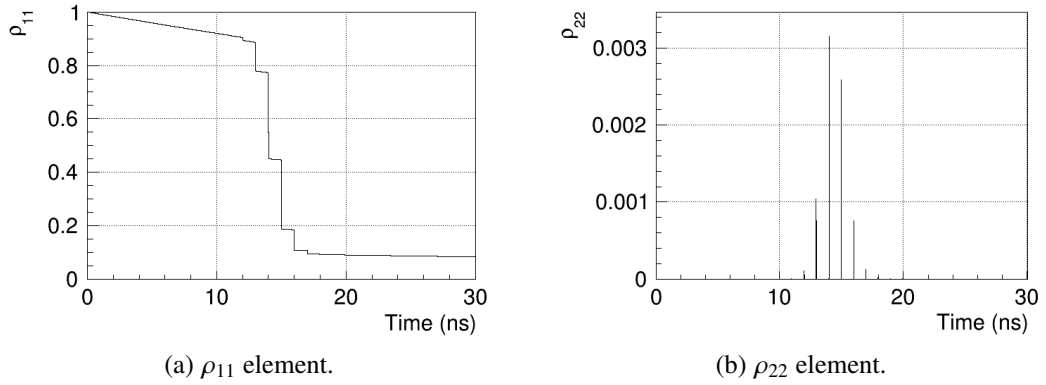
Figure 3.18: Example of density matrix by the model calculation of the Ps excitation.

An example of the calculations based on the model is shown in Figure 3.18 for the density matrix elements, and Figure 3.19 for Γ_L, which is the increased intensity of annihilation γ-rays by the enhanced decay. The envelope of Γ_L has a Gaussian timing profile with the same width as the laser power profile. Here the integration of the increased decay rate was defined to be I_L. Γ_L can therefore be formulated as

$$\Gamma_L(t) = \frac{I_L}{\sqrt{2\pi}\sigma_L} \exp\left(-\frac{t - t_L}{2\sigma_L^2}\right). \tag{3.10}$$

t_L represents timing of irradiation of the laser, and σ_L is a width of the profile. Probability for Ps to decay by laser irradiation can be calculated as $1 - \exp(-I_L)$ by this parametrization. I_L and corresponding probability to decay are calculated for various wavelengths of the laser and Γ_2 as shown in Figure 3.20. Broad resonance spectra with the natural line width were reproduced by the model. Resonance spectra were modeled by Voigt functions, which were convolutions of Gaussian and Breit Wigner functions, to be used in analysis. Γ_L linearly depended on the pulse energy and $1 - P_1$. These dependence are used to estimate systematic uncertainties.

50
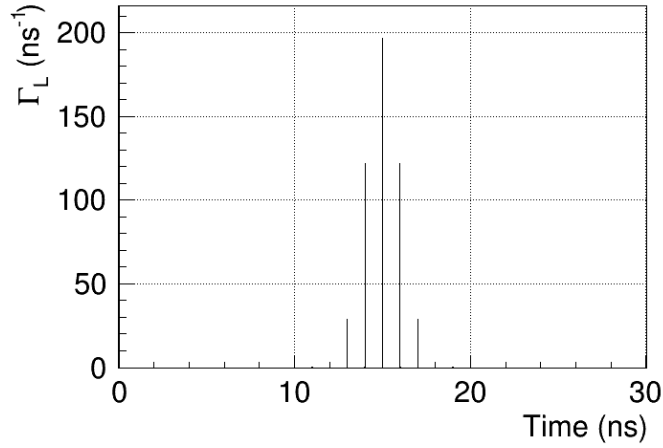
Figure 3.19: Example of Γ_L by the model calculation of the Ps excitation.
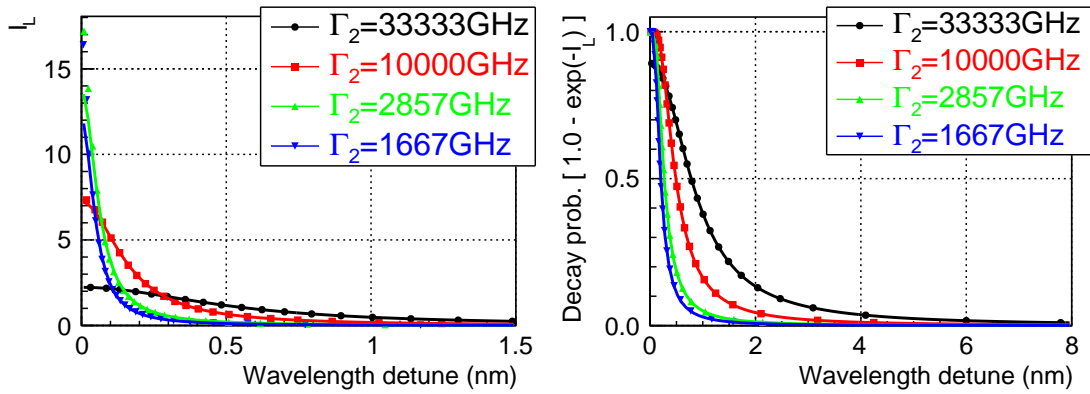
Figure 3.20: Resonance spectra of integrated decay rate I_L (left) and corresponding probability to decay (right). The points were results of the calculations, and the curves were modeled Voigt functions to be used in analysis. Broad resonance spectra with the natural line width were reproduced by the model.

Chapter 4

Results and discussion

Results of the measurements of the decay rate of 2P-Ps (Γ_2) confined in the pores are reported and discussed in this chapter. In contrast to be in vacuum, the enhanced decay and the broad resonance spectrum were observed in the silica aerogels' pores where 1S-Ps did not form the surface state. This observation favors that some of the distinctive features of the 2P state induce the abnormal phenomena. Γ_2 was measured to be in the order of 1 THz in the measured range of Ps kinetic energy (0.04 eV–0.2 eV). The decay rate can be interpreted as the decay process occurred in almost every collision with the material, and had a resonance around Ps kinetic energy of 0.06 eV. The broadening was observed independently on Γ_2 as wide as around 1 nm in FWHM. Possible mechanisms of the broadening and the enhanced decay, and future directions of studying them are discussed.

4.1 Demonstration of Ps Lyman-α transition in vacuum

The Lyman-α transition of Ps in vacuum was demonstrated to confirm that the system was able to excite Ps into the 2P state and then ionize it to detect annihilation γ-rays from the dissociated positron. The silica aerogel without the cap was used to let o-Ps escape in the outer vacuum of the pores, and the UV excitation laser and the green ionization laser were irradiated on the escaped o-Ps.

Annihilation γ-rays from the dissociated slow positrons were observed in a largely delayed timing region. Figure 4.1 show the timing spectra and energy spectra of the delayed γ-rays emitted after 700 ns from the irradiation of the positrons. The wavelength of the UV laser was set to be 243.0 nm for this measurement. An intensity of the very slow component after around 1000 ns increased by the laser irradiations because the dissociated positrons were so slow to take such a long time to hit the surrounding materials. The decay mode of the slow component was confirmed to be the 2γ mode from the 511 keV total absorption peak in the energy spectrum. This agreed with the expected poor production of the long lived o-Ps in the majority of surrounding materials of the chamber.

The transition signal was not observed without the green laser, or with detuned wavelengths of the UV laser. The timing spectrum by irradiating the UV laser alone is shown in Figure 4.2, and the signal of the transition scanned against wavelength of the UV laser is shown in Figure 4.3.

53
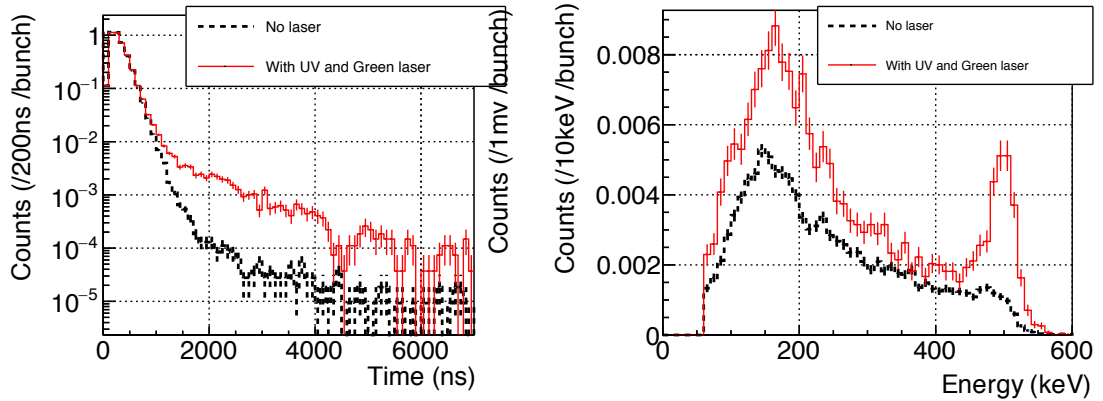
Figure 4.1: Timing (left) and energy (right) spectra of annihilation γ-rays from Ps excited in vacuum. An intensity of the very slow component after around 1000 ns increased by the laser irradiations. The decay mode of the slow component was confirmed to be the 2γ mode as expected.

The lack of the signal without the green laser and the resonance at 243 nm are good evidences of the successful demonstration of the designed processes in which the laser irradiations induced Ps Lyman-α transitions and the following ionizations.

A Gaussian function was fitted to the resonance spectrum, and the width was 0.21 nm in FWHM. Assuming that the width was from Doppler broadening, the mean kinetic energy of Ps was estimated as 0.20 eV, which corresponded to 1.5×10^3 K. The energy was reasonable from the expected thermalization process as shown in Figure 3.10. The enhanced decay and the broadening were not observed if Ps was excited in vacuum.

4.2 Observation of the enhanced decay and the broadening for confined 2P-Ps

The enhanced decay of Ps into annihilation γ-rays was observed by irradiating the UV laser alone on Ps confined in the aerogel with the cap. Figure 4.4 shows waveforms of the PMT outputs with and without the UV laser irradiation, and the differential waveform. Only UV laser (485 μJ pulse energy at the sample, 243.0 nm wavelength) was irradiated at 310 ns delayed from the positrons. An instance increase of the annihilation γ-rays was observed just after the laser irradiation. γ-rays emitted after around 370 ns decreased because less 1S-Ps remained. The enhancement of the decay was so strong that around 50 % of Ps decayed as obvious from a timing spectrum by the pulse-by-pulse analysis, which is shown in Figure 4.5. The energy threshold of 240 keV was set to produce the spectra. The increase of the annihilation γ-rays at the timing of the laser irradiation was also observed, and the intensity after the increase became around the half of that without the laser. In the following subsection 4.2.2, the timing profile of the γ-rays enhanced by the laser and the quantitative consistency between the increased and the decreased

54
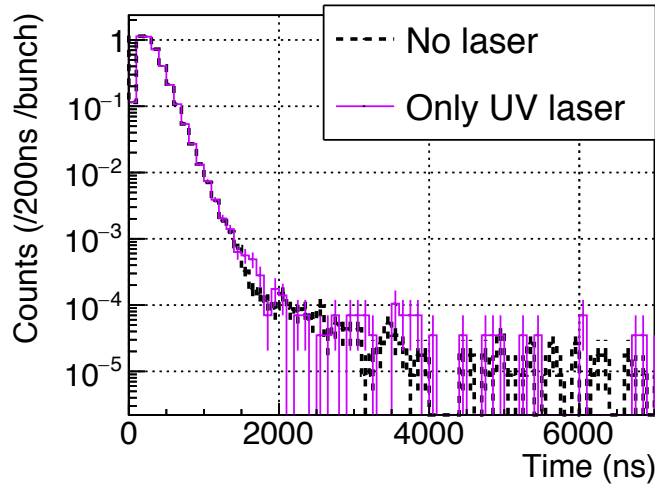
Figure 4.2: Timing spectrum by irradiating only UV laser on Ps in vacuum. The increase of the delayed component was not observed.
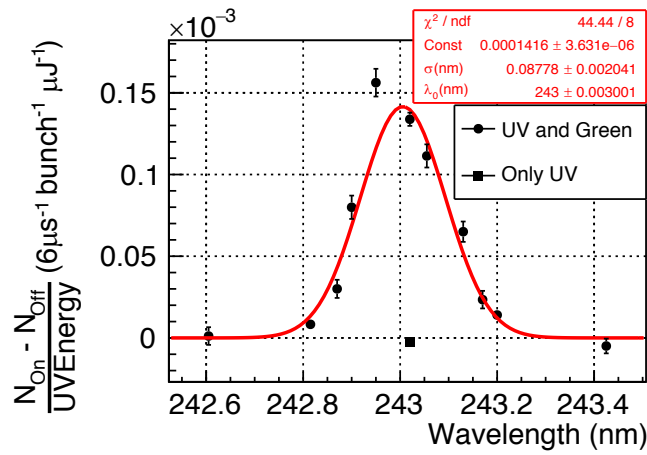
Figure 4.3: Resonance spectrum of Ps Lyman-α transition in vacuum. The center of the resonance was reasonable for the Lyman-α, and the width agreed with that of Doppler broadening by temperature of 1.5×10^3 K, which can be reasonably assumed from the thermalization process.

55
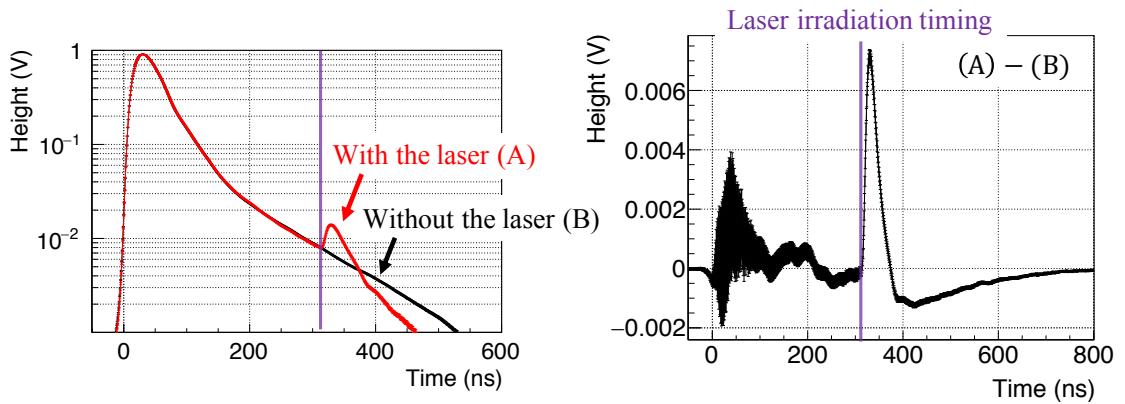
Figure 4.4: (Left) Waveforms with and without the UV laser. (Right) Differential waveform generated by subtracting the waveform without the laser from that with the laser. Annihilation γ-rays were increased just after the laser irradiation.

Parameters from the MC		Result of the fitting	$\pm$(stat.) $\pm$ (sys.)
		χ^2/ndf	$104/72$
		N_{oPs} at 296 ns	$25.8 \pm 0.6 \pm 0.5$
		Γ_{po}	$0.8 \pm 0.1 \pm 3 \times 10^{-6}\,\mu s^{-1}$
ε_3 over 240 keV	1.59 ± 0.04 %	I_L	$0.74 \pm 0.03 \pm 0.04$
ε_2 over 240 keV	1.47 ± 0.03 %	σ_L	$1.05 \pm 0.04 \pm 0.003$ ns
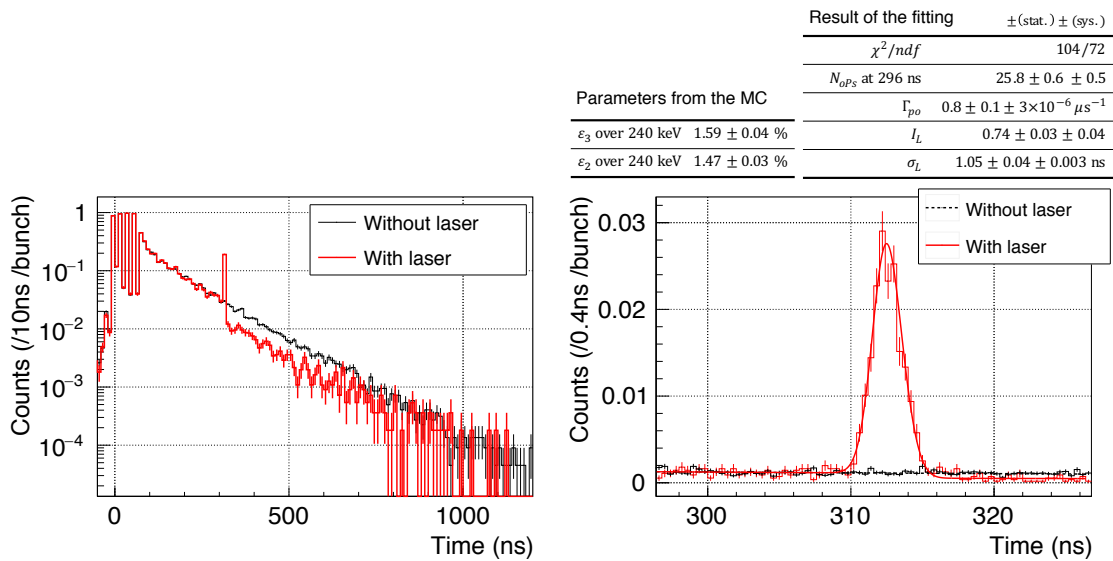
Figure 4.5: Timing spectra of the γ-rays increased by the UV laser. (Left) In a long time range. (Right) Focused at the laser irradiation timing. γ-rays enhanced by the laser were emitted by pulse shaped timing profile. The spectra were fitted by the decay model to yield parameters summarized in tables in the figure. The reproduced curves are superimposed.

56
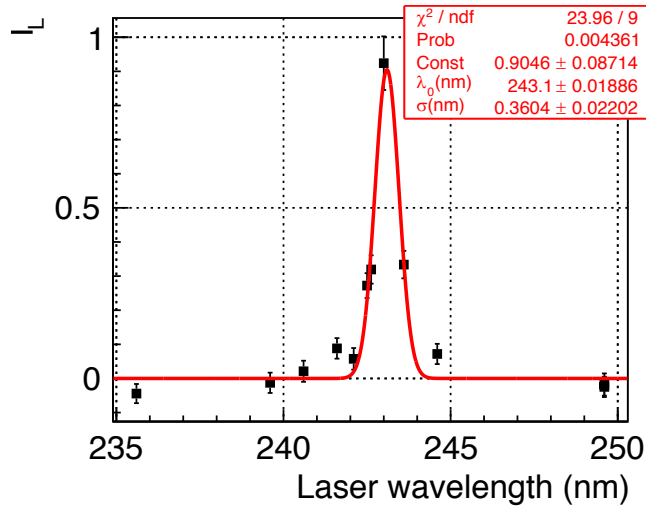
Figure 4.6: Resonance curve of I_L in wide range of wavelength. The enhanced decay had the resonance at Ps Lyman-α (243 nm) and the width was broad as 0.8 nm in FWHM. Doppler broadening or the collisional broadening was not able to naively explain this broad width by the reasonable kinetic energy of Ps.

intensity are studied in detail by applying the decay model of Ps in section 3.4.

The enhanced decay was observed at the resonance of the Lyman-α, and the width was also broadened as observed in the previous work [2]. Figure 4.6 shows a dependence of I_L scanned in a wide range of wavelength of the UV laser. I_L were estimated so that $1 - \exp(-I_L)$ represented the decayed ratio of Ps by the UV laser. The enhanced decay had the resonance at Ps Lyman-α (243 nm). This feature of the resonance favors that the UV laser induced Lyman-α transition rather than active centers, which could quench Ps, on the pore surface of the aerogels, because the silica aerogels did not have a resonance structure at the wavelength of Ps Lyman-α in light absorption spectra as described in subsection 2.2.6. The resonance spectrum was fitted by a Gaussian function to estimate the width as broad as 0.85 nm in FWHM. The width was too broad to be naively attributed to Doppler or the collisional broadening. The mean kinetic energy of Ps to explain the broad width by those effects is more than 3 eV, which is not consistent with the thermalization process in the aerogel. The broadening should be caused by other effects induced by the material.

From the above observations, it was concluded that even in the aerogel the decay of 2P-Ps was enhanced and the resonance spectrum was abnormally broadened. Because the lifetime of 1S-Ps in the aerogel agreed with the prediction of the RTE model, it was expected that 1S-Ps did not form the surface state. The mechanisms of the enhanced decay and the broadening should be related to some of the distinctive features of the 2P state. Measurements of the dependences on Ps kinetic energy of the enhanced decay rate and the broadening are reported in section 4.3, which will be useful to identify physical mechanisms. The dependences were measured by scanning the timing of the irradiation of the UV laser. The kinetic energy was estimated to be ranged in 0.04 eV–0.2 eV as shown in Figure 3.10. The following subsections discuss the decay mode of
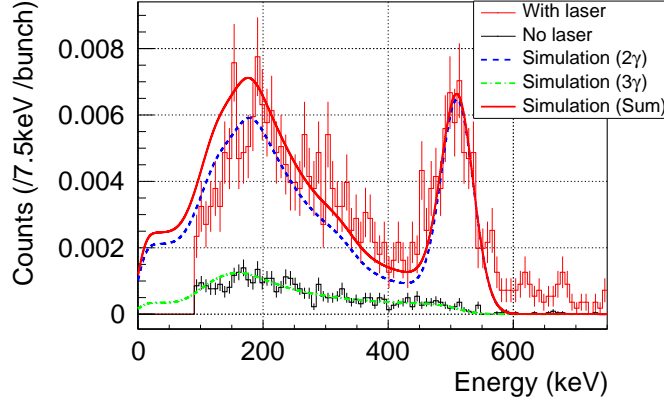
Figure 4.7: Energy spectra of γ-rays emitted around the laser irradiation. Because the total absorption peak of 511 keV γ-rays was clearly observed for the enhanced decay by the UV laser, it was assumed that the decay of 2P-Ps was fully in the 2γ mode.

2P-Ps and the application of the decay model, which are used in the quantitative analysis.

4.2.1   Decay mode of the confined 2P-Ps

A dominant decay mode of the confined 2P-Ps was confirmed to be the 2γ mode from an energy spectrum of γ-rays enhanced by the laser. Figure 4.7 shows energy spectra of γ-rays detected in a ± 3 ns timing region around the laser irradiation. The total absorption peak of 511 keV γ-rays was clearly observed for the enhanced decay by the UV laser. Higher energy signals than the total absorption might be recorded due to the residual pileups, which could also cause the disagreement of spectra between the measurement and the simulations. The decay mode of the confined 2P-Ps was assumed to be in fully 2γ mode hereafter.

4.2.2   Adaptability of the decay model

Adaptability of the decay model of Ps described in section 3.4 was confirmed by applying the model to measured data. First, the timing profile of the enhanced γ-rays is inspected. In the right of Figure 4.5, the fitted model function is superimposed on the timing spectrum. While fitting to the data with laser, N_{oPs} and Γ_{po} were fixed by those acquired from the data without laser. The laser enhanced γ-rays were confirmed to have a pulse like shape, which originated from the timing profile of the pulse laser as expected by the model. The timing width of the laser enhanced decay, σ_L, was estimated as $\sigma_L = 1.05 \pm 0.04(\text{stat.}) \pm 0.003(\text{sys.})$ ns, which was $2.47 \pm 0.09(\text{stat.}) \pm 0.007(\text{sys.})$ ns in FWHM. Here the systematic uncertainty from the MC simulation is quoted. The width was much wider than the achieved timing resolution (0.64 ns FWHM) described in section 3.2. The contribution from an intrinsic timing profile of the enhanced decay was estimated as 2.39 ns by subtracting the resolution. This width reasonably agreed with the possible pulse duration of the UV laser, which is explained in section 2.3. The model was able to describe the timing profile of the laser enhanced γ-rays.

Parameters from the MC

ε_3	9.3 ± 0.4 keV
ε_2	8.4 ± 0.4 keV

Result of the fitting	$\pm$(stat.) $\pm$ (sys.)
p-value	0.20
N_{prompt}	$1675 \pm 2 \pm 76$
N_{oPs}	$346 \pm 1 \, ^{+8}_{-14}$
Γ_{po} after 240 ns	$1.13 \pm 0.07 \pm 0.02 \; \mu s^{-1}$
I_L	$0.72 \pm 0.03 \, ^{+0.01}_{-0.02}$
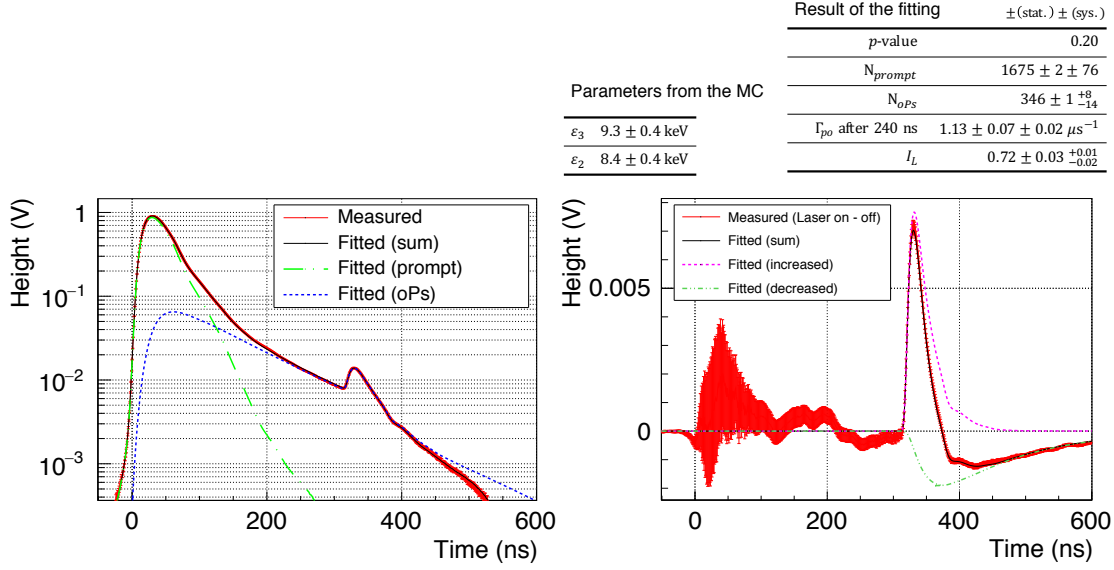
Figure 4.8: (Left) Waveform with laser. (Right) Differential waveform. The reproduced waveforms are superimposed with decomposed into components. The increase and the decrease in the differential waveform was consistent each other. The reproduced differential waveform was obtained by subtracting reproduced waveform without laser from that with laser, and decomposed into the increase and following decrease of 1S-Ps decay. Parameters in the model are summarized in tables in the figure.

The consistency between the increased γ-rays from 2P-Ps and the decreased γ-rays from less remained 1S-Ps was also confirmed. In the pulse-by-pulse analysis, the ratio between increased and decreased counts was determined by the detection efficiencies estimated by the Monte Carlo simulation. As shown in Figure 4.5, both of the increase and the decrease were consistently reproduced. I_L was estimated as $I_L = 0.74 \pm 0.03$(stat.) ± 0.04(sys.), which corresponded that 52 ± 2(stat.) ± 2(sys.) % of remained Ps at the timing of the laser irradiation decayed into γ-rays.

This consistency between the increase and the decrease was also confirmed by the SSPALS analysis. Figure 4.8 (left) shows results of fitting the reproduced waveform to the measured waveform with laser, and Figure 4.8 (right) shows the differential waveform and the corresponding reproduced waveforms. N_{oPs} and Γ_{po} before the laser irradiation were also fixed by analyzing the data without laser while Γ_{po} after the irradiation of the laser were set to be free parameters. σ_L was fixed to that from the pulse-by-pulse analysis because the response function of the detector, which was used in the SSPALS analysis, had much wider width than σ_L. The waveforms were also well reproduced by the SSPALS analysis. The reproduced differential waveform in Figure 4.8 (right) was decomposed into increased (S_{inc}) and decreased (S_{dec}) components defined

by the following equations:

$$S_{inc}(t) = \varepsilon_L \Gamma_L(t) N_{oPs} \exp\left(-\int_0^t (\Gamma_{po}(t') + \Gamma_s + \Gamma_L(t'))dt'\right),$$ (4.1)

$$S_{dec}(t) = -(\varepsilon_2 \Gamma_{po}(t) + \varepsilon_3 \Gamma_s) N_{oPs} \exp\left(-\int_0^t (\Gamma_{po}(t') + \Gamma_s)dt'\right)\left(1 - \exp\left(-\int_0^t \Gamma_L(t')dt'\right)\right).$$ (4.2)

S_{inc} represents the increased intensity by decays of 2P-Ps, and S_{dec} represents the decreased intensity from self decays of remained 1S-Ps. Both components are superimposed in the figure to easily understand how each component contributed the resulted waveform. I_L was estimated as $0.72 \pm 0.03\text{(stat.)} ^{+0.01}_{-0.02}\text{(sys.)}$, which was consistent with the pulse-by-pulse analysis. In the SSPALS analysis, the systematic uncertainty from the estimation of the timing profile of the positrons was also evaluated. The decay model was able to describe the enhanced decay of 2P-Ps, and the both analysis methods were able to yield consistent results.

4.3 Quantitative analysis of the broadening and the decay rate

4.3.1 Estimations of the width of the broadening and the decay rate

The decay rate of the confined 2P-Ps, Γ_2, was estimated by comparing measured resonance spectra by the model. Resonance spectra were measured by irradiating laser at different timings. Because 1S-Ps had the time dependent mean kinetic energy through the thermalization process, it was expected that the mean kinetic energy of 2P-Ps at the excitations was able to be varied by changing the timing of the laser irradiation (t_L). Figure 4.9 shows the resonance spectra measured with fine steps of the wavelength, and a result of scanning t_L at the center of the resonance. The resonance spectra were obtained with 330 μJ, and the timing scan with 485 μJ pulse energy of the UV laser at the sample. The results from the SSPALS analysis are shown here.

At every t_L the similar broad line widths as wide as 1 nm in FWHM were observed as in the previous work [2], but the peak I_L were not uniform. The assumed model is not able to describe these behaviors without a modification because the line width and the peak value correlate each other as shown in Figure 3.20. It implies that an inhomogeneous broadening takes effect in the aerogel. A Gaussian shape profile was introduced to model the broadening effect, whose possible origin is discussed later in subsection 4.4.1. Observable resonance spectra were obtained by calculating averaged I_L from the intrinsic resonance spectra and the broadening profile. Since the intrinsic resonance spectra depend on Γ_2, Γ_2 and the width of the broadening σ_B were able to be determined by globally fitted to the measured data. Because the data showed that I_L decreased in time from around $t_L = 90$ ns, it is implied that Γ_2 decreased from a certain Ps kinetic energy. Γ_2 is modeled by a toy function of the energy E as

$$\Gamma_2(E) = \frac{\Gamma_M}{1 + \exp(-(E - E_{th})/E_b)}.$$ (4.3)

The four parameters are estimated by fitted to the measured data.
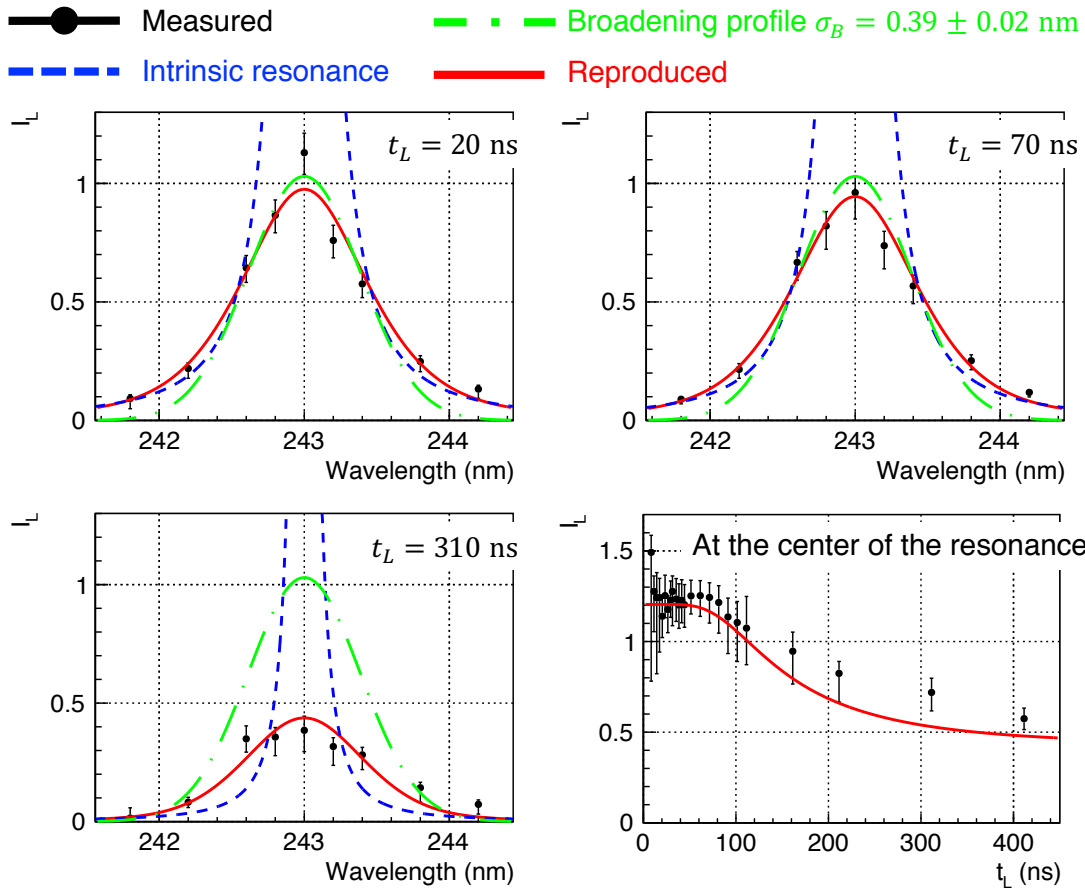
Figure 4.9: Resonance spectra and timing scan of I_L. The reproduced curves were obtained by averaging the intrinsic resonance spectra over the broadening profile. The same width of the broadening profile was used for all curves.

Table 4.1: Sources of uncertainties related with measurements and analysis, and their effects for estimating I_L. The largest effect is quoted for the source whose effect significantly depended on t_L or wavelength of the laser.

Source	Uncertainty of the source	Effect on I_L
Statistics		$\pm 2\%$
Detection efficiencies	2%	$\pm 2\%$
Estimation of the timing profile of the positrons	Described in section 3.3.1	$+0\%/-40\%$ for $t_L = 8$ ns
Deviation from the pulse-by-pulse method	Described in subsection 4.3.4	-40% in maximum for $t_L = 310$ ns and wavelength of 244.2 nm. Typically $\pm 10\%$.

Table 4.2: Sources of uncertainties related with the decay model, and their effects for estimating I_L. The largest effect is quoted for the source whose effect significantly depended on t_L or wavelength of the laser.

Source	Uncertainty of the source	Effect on I_L
Jitter of pulse energy of the UV laser	6%	$\pm 6\%$
Misalignment between the laser and the positrons	1 mm	$\pm 7\%$
Estimation of kinetic energy of Ps	Shown in Figure 4.10 and Figure 4.11	$\pm 12\%$ for $t_L = 210$ ns

Uncertainties shown by error bars in Figure 4.9 were used as inverses of the weights for the least squares fitting. Contributions from statistical and systematic uncertainties are combined. Sources of uncertainties and their effects for estimating I_L are summarized in Table 4.1 and Table 4.2. The uncertainty of kinetic energy of Ps was evaluated from the discrepancy between the expected and measured time evolution of the pick-off decay rate shown in Figure 3.10. A range of the uncertainty of the energy was determined to reasonably include measured pick-off decay rates. Figure 4.10 shows the range of the uncertainty. Measured pick-off decay rates were converted into the kinetic energy according to the RTE model. Figure 4.11 show magnified views in different ranges.

σ_B and parameters to describe $\Gamma_2(E)$ in Equation 4.3 were estimated by fitted to the measured data in Figure 4.9. Fitted resonance spectra and timing dependence of the peak I_L are superimposed in Figure 4.9, and resulted $\Gamma_2(E)$ is shown in Figure 4.12. The time duration of the laser pulse in the model was set to reproduce measured σ_L. Γ_2 was estimated to be
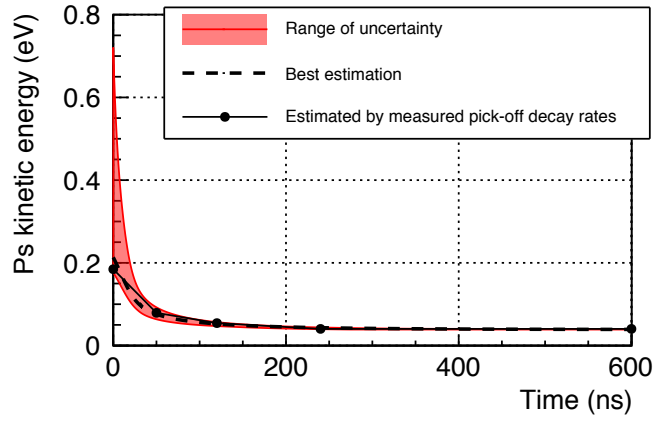
Figure 4.10: Uncertainty of time evolution of Ps kinetic energy. The range of the uncertainty was determined to reasonably include measured points.
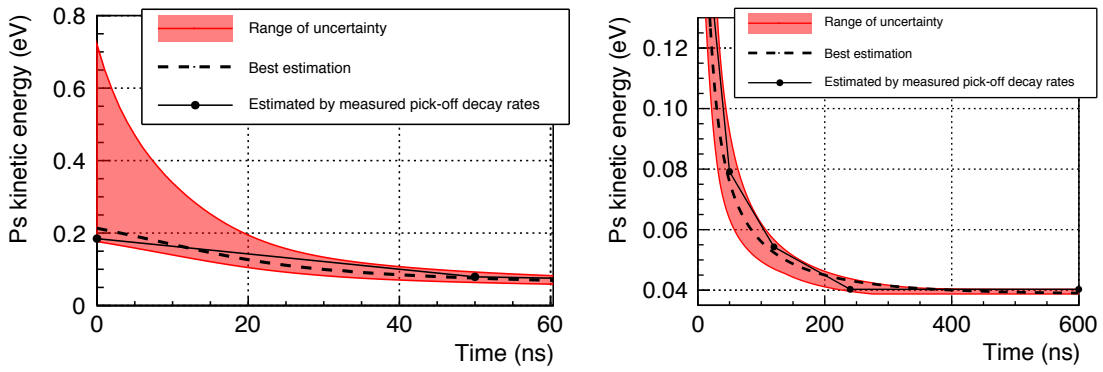
Figure 4.11: Magnified views of the uncertainty of time evolution of Ps kinetic energy.

Result of the fitting

Γ_M	$(6.8\,^{+0.8}_{-0.6})\times 10^3$ GHz
E_{th}	$(5.0\,^{+0.3}_{-0.4})\times 10^{-2}$ eV
E_b	$(5.8\,^{+1.9}_{-2.7})\times 10^{-3}$ eV
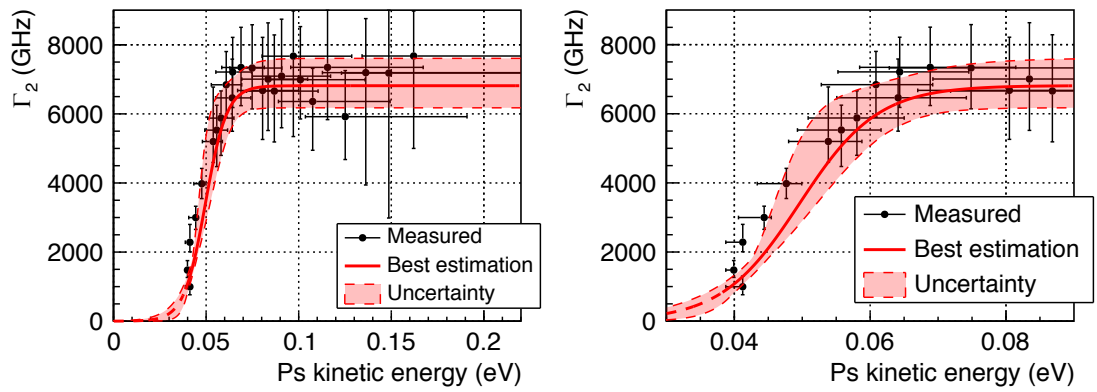
Figure 4.12: Resulted $\Gamma_2(E)$ and the measured points. The right figure magnifies around the point from which the decay rate started to decrease.
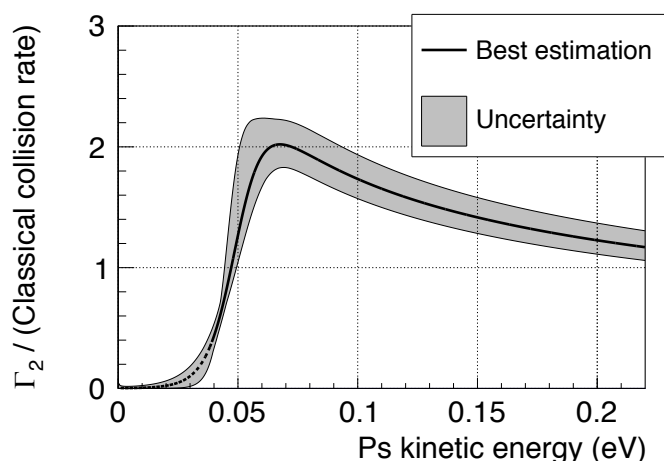
Figure 4.13: Energy dependence of the decay probability of per a collision. The classical collision rate was assumed by $\overline{L}/v$ where v was velocity. The resonance around 0.06 eV was observed. The dashed line was in an extrapolated region where data did not exist.

$(6.8 + 0.8/-0.6) \times 10^3$ GHz in maximum and start to decrease from around 0.06 eV down to around 1 THz for the thermalized Ps. The line width was broadened as wide as 0.39 ± 0.02 nm in one sigma, which corresponded to 0.92 ± 0.05 nm in FWHM.

A decay probability per a collision in the pores can be estimated from $\Gamma_2(E)$. A rate of collision was classically assumed to be $\overline{L}/v$ where $\overline{L} = 34$ nm as the mean free path in the pores, and v is velocity of Ps. Figure 4.13 shows the calculated probability against Ps kinetic energy. The probability was in the order of unity. It can be interpreted that the decay occurred in every collision with the pore surface. The probability had the peak at around 0.06 eV. This implies that a bound state was possibly formed between 2P-Ps and the surface as discussed in subsection 4.4.2.

4.3.2 Dependence of the enhanced decay on radicals induced by the UV laser

The quenching of o-Ps by radicals induced by the UV laser was observed during the measurements, but the amount of the radicals did not affect the enhanced decay of 2P-Ps. As described in section 1.1.2, the radicals were increased in time by irradiating the UV laser on the aerogels. Figure 4.14 shows the timing spectra measured at different accumulations of the radicals. Measurements of the resonance spectra by scanning the wavelength were performed after scanning the timing of the laser in fine steps at the center of the resonance. The decrease of o-Ps by the accumulations of radicals was clearly observed. N_{oPs} decreased and Γ_{po} increased by around 25 % in the wavelength scan compared with during the timing scan, but observed I_L decreased as shown in Figure 4.9. This decrease was able to be explained by the decrease of the pulse energy of the UV laser between scans. Calculations including the decrease of the pulse energy were able to globally explain the both scans shown in Figure 4.9. The radicals induced by the UV laser had less effects on the decay of 2P-Ps.
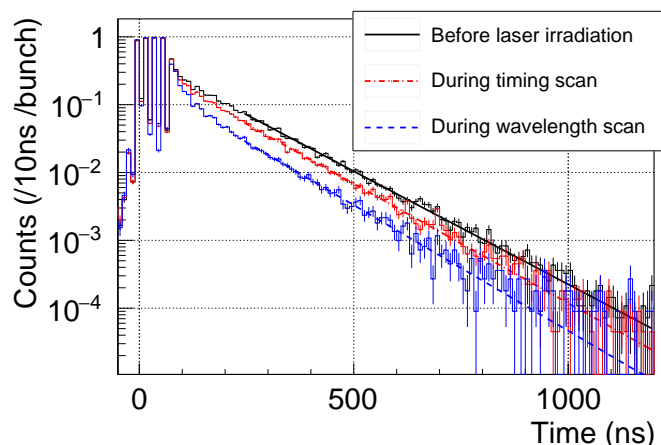
Figure 4.14: Timing spectra measured at different accumulations of the radicals. More radicals were accumulated during the wavelength scan, and they quenched o-Ps to reduce N_{oPs} and increased Γ_{po} by around 25 %.

4.3.3 Less pick-off decay by the energy selective decay of 2P-Ps

Decreases of the pick-off decay rate after the irradiations of the UV laser were observed because of the larger Γ_2 for more energetic Ps. The left of Figure 4.15 compares the pick-off decay rates with and without the laser irradiations, and the right shows an example of the timing spectra, which was acquired with $t_L = 160$ ns. The pick-off decay rates were calculated by the pulse-by-pulse analysis. The fittings to estimate the pick-off decay rates were performed from 240 ns or later than t_L. As shown in the right of Figure 4.15, the slope of the spectrum became more flat with the laser. This means that the less pick-off occurred after the irradiation of the laser. The pick-off decay rate averaged over t_L decreased by 28 ± 5 % from $1.06 \pm 0.02\,\mu s^{-1}$ to $0.76 \pm 0.05\,\mu s^{-1}$. The dependence of Γ_2 on the kinetic energy is able to explain the decrease of the pick-off decay rate since more energetic Ps is more probable to decay in the 2P state to result in the less pick-off decay for the remained 1S-Ps. Figure 4.16 shows a calculated variation of the energy distributions by the energy selective decay of 2P-Ps with assuming $\Gamma_2(E)$ in Figure 4.12. The distribution without the laser was assumed to be Maxwell-Boltzmann distribution with 380 K to simulate data by $t_L = 160$ ns. The mean energy was estimated to decrease by 25 % from 0.049 eV to 0.037 eV. This deceleration can consistently explain the decrease of the pick-off decay rate, which is almost linear function of the kinetic energy as described in Figure 1.4.

4.3.4 Consistency between the analysis methods

The consistency of the results by the two analysis methods was checked. Figure 4.17 compares resonance spectra and timing dependence of I_L obtained by both of the methods. Error bars of the points hereby represent only uncertainties summarized in Table 4.1, which are related with measurements and analysis, to see deviations by analysis methods. In the pulse-by-pulse analysis, I_L were estimated by fitting the decay model to the data from 240 ns or later than t_L
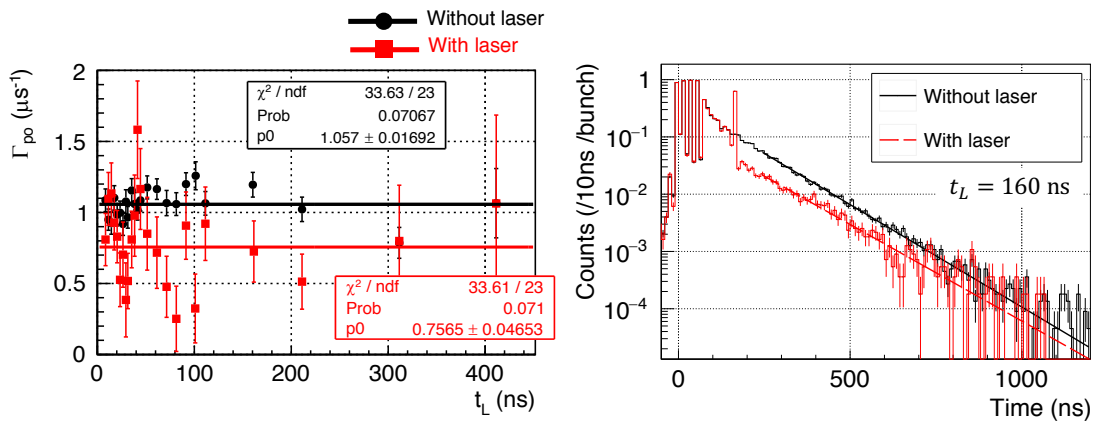
Figure 4.15: Decreases of the pick-off decay rates by energy selective 2P-Ps decay. (Left) Pick-off decay rates for various t_L. (Right) Example of the timing spectra. The spectrum was obtained with $t_L = 160$ ns. The less steep slope was observed with the laser. This is the result of the energy selective decay of 2P-Ps.
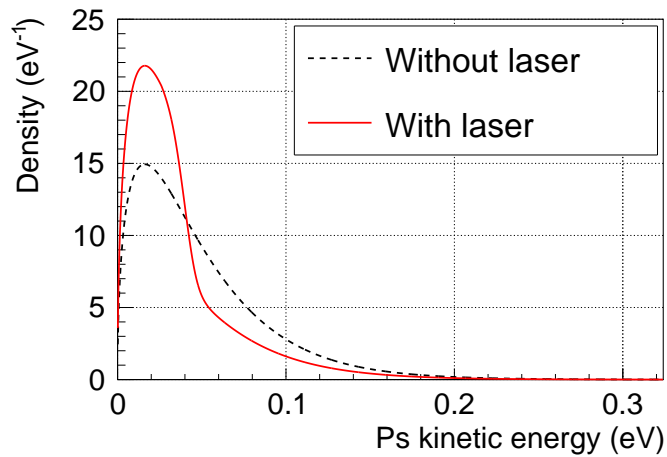
Figure 4.16: Decrease of kinetic energy by energy selective 2P-Ps decay. The decrease of the pick-off decay rate was able to be explained by the deceleration.
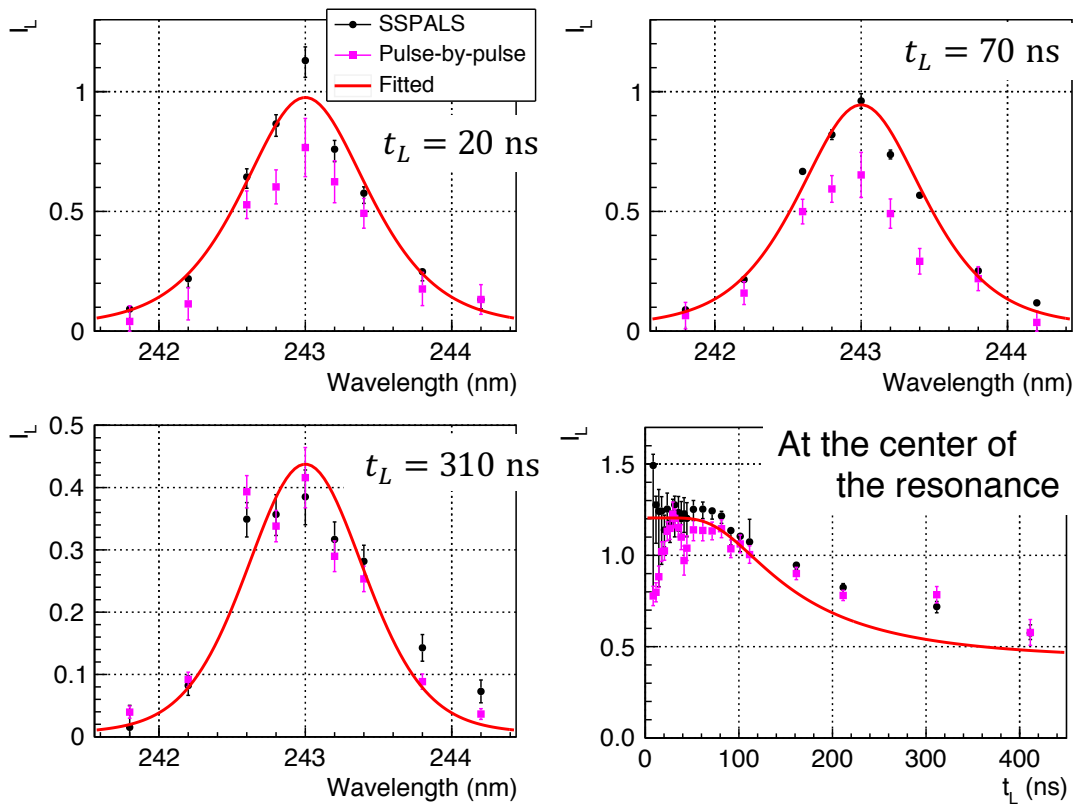
Figure 4.17: Comparisons of the resonance spectra and the timing dependence of I_L. Both results agreed at later t_L, and the same tendency of the dependence of Γ_2 on the kinetic energy was observed. Disagreements could be explained by inevitable systematic errors from the extrapolation in the pulse-by-pulse analysis.

in order to estimate N_{oPs} and Γ_{po}, and then extrapolating the model function to estimate N_{oPs} at t_L. Both results agreed at later t_L, and the same tendency of the dependence of Γ_2 on the kinetic energy was observed. The lower I_L at early t_L by the pulse-by-pulse analysis could be obtained by a systematic error from the long extrapolation. For t_L before 30 ns, not all of the positrons in the beam were arrived at the timing of the laser irradiation to result in the spurious decrease of the estimated ratio of decayed Ps. The results after $t_L = 30$ ns were also lower by around 10 % than the SSPALS method. This could be attributed to the decrease of Γ_{po} by the energy selective decay, because the effect of the extrapolation would become different. It is assumed from Figure 3.10 that Γ_{po} is twice as large as the thermalized value during 100 ns from the productions of Ps. N_{oPs} could be systematically lower by the extrapolation using $\Gamma_{po} \simeq 1 \, \mu s^{-1}$, which was typically estimated by analyzing data without laser. The effect is evaluated as large as 10 % for N_{oPs} by $\exp((2\Gamma_{po} - \Gamma_{po}) \times 100 \, \text{ns}) - 1 = 0.10$. Because of this systematic error which can appear at early t_L in the pulse-by-pulse analysis, estimations described in subsection 4.3.1 were based on the SSPALS analysis. Deviations between the two methods were included into the uncertainties for data at $t_L > 240$ ns, where the extrapolation was not performed.

4.4 Discussion

It is necessary to suppress the broadening and the decay process in order to realize the proposed efficient cooling scheme. Following the observations, possible directions are discussed to elucidate mechanisms of each phenomenon. Outlook for realizing the rapid cooling by suppressing phenomena is also discussed.

4.4.1 Broadening effect

In the present measurement, the broadening as large as 1 nm was observed and independent on the decay rate. This implies that the broadening is caused by other mechanisms than those which induce the decay process. One of the promising mechanisms is that a variation of residual electric fields in the pores caused the position dependent DC Stark shift on the 2P state energy levels. The broad resonance spectrum is obtained because the position of Ps at the excitation should be random in the pores. Shifts of binding energy of the 1S and 2P states are calculated against strength of the electric field as shown in Figure 4.18. A strength of the electric field to cause the shift on the energy interval as large as 1 nm can be calculated as around 400 kV/cm.

This field value is reasonably expected by contributions from remaining dipole moments of silanol groups ($-Si(OH)$) on the surface of nano particles of which the hydrophobic silica aerogel consists. Figure 4.19 shows a schematic drawing of silica nano particles with its chemical groups [52]. A typical powder of hydrophobic fumed silica is known to have the remaining silanol groups as dense as $\sigma = 0.44 \, \text{nm}^{-2}$ [53]. If Ps is trapped in pores, a squared mean field which Ps effectively feels can be calculated as [52]

$$E^2 = \frac{\pi \sigma p^2}{2\overline{L}\epsilon^3},\tag{4.4}$$

where $p = 0.050 \, \text{Vnm}^2$ is the dipole moment of $-OH$ groups, $\overline{L}$ is a mean distance between
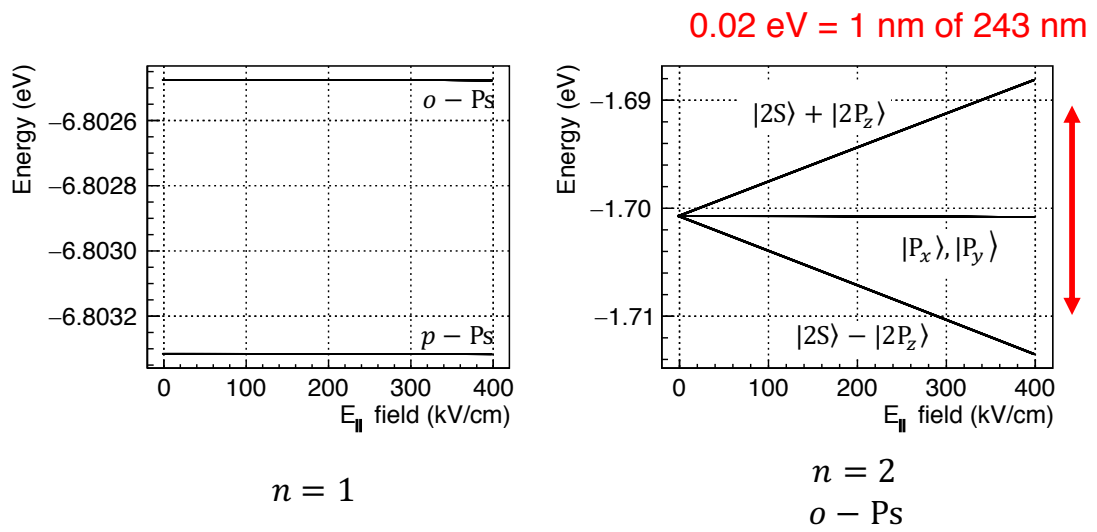
Figure 4.18: Calculated shifts of the binding energy of Ps under electric field. Perturbed states are shown by legends in the figure. Suffixes x, y, and z show the magnetic quantum state, where z is the direction of the electric field. The broad width can be observed under around the field of $400\,\mathrm{kV/cm}$.
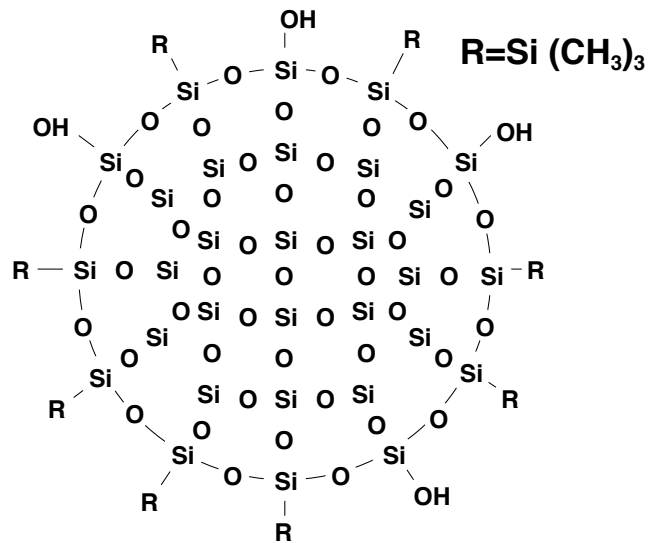
Figure 4.19: Schematic drawing of silica nano particles with its chemical groups [52]. The surface is mainly modified by trimethyl ($-\mathrm{Si(CH_3)_3}$) groups to be hydrophobic, but a certain amount of silanol groups are known to remain.
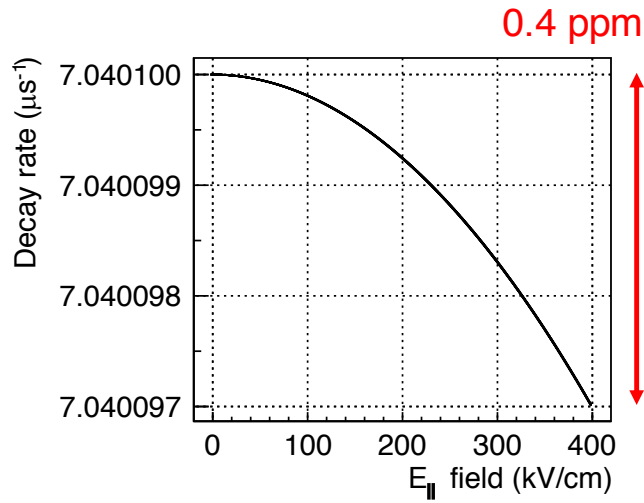
Figure 4.20: Calculated shifts of the self decay rate of o-Ps under electric field. The decay rate shifts only 0.4 ppm, which is not measurable in the current precision.

grains consisting of pores, and ϵ is a minimum distance between the grain and Ps. By substituting $\overline{L}$ = 34 nm and ϵ = 0.4 nm, which is Bohr radius of 2P-Ps, the field can be evaluated as $\sqrt{E^2} \simeq 280$ kV/cm. The field is in the order of the strength to induce the observed broad width of the resonance spectrum.

A consistency between the existence of such strong field and the precise measurement of the lifetime of o-Ps in silica aerogels was checked. Figure 4.20 shows a calculated shift of the self decay rate of o-Ps under electric field. The decay rate shifts only 0.4 ppm, which is not measurable in the current precision.

This assumption that the residual electric field broadens the resonance spectrum can be verified by performing spectroscopy for atoms confined in the silica aerogel, while material effects especially on the probe system should be clarified beforehand [54, 55]. For example, broad Raman spectrum was observed for caffeine molecule confined in a mesoporous silica material[55]. Systematic studies using well understood and simple systems will be beneficial to elucidate the effects from the material.

4.4.2 Decay process

The decay of 2P-Ps was enhanced through possibly forming the bound state whose resonance was at around 0.06 eV. While a lot of resonant annihilations of positrons with various atoms and molecules have been reported for low energy positrons down to around 0.1 eV [56], there are limited reports of the quenching of Ps with forming a bound state with other systems. For example, gases such as NO_2, Br_2, and I_2 are known to quench o-Ps in the 1S state with high probability [57–59]. It was suggested that the quenching occurs through forming bound states with those molecules, and can be resonant if the bound states are unstable [59]. A reason by which the quenching occurs with only those molecules is proposed to be the small bond strengths [58],

but mechanisms are still unclear to my knowledge. The enhanced decay which was observed in the present work can be the similar quenching phenomenon. Theoretical studies including specific properties of materials will be beneficial to elucidate the quenching phenomena.

Because the enhanced decay was observed only for 2P-Ps and less affected by the radicals in the present work, some of the distinctive features of the 2P state induce the enhanced decay. First, the binding energy in $n = 2$ state is small by 5.1 eV compared with the 1S state. If the work function of 2P-Ps to silica is assumed to be same with that for 1S-Ps, which is assumed to be in from -3 eV to -1 eV, 2P-Ps is naively expected to have the positive work function to penetrate into the bulk of silica and be dissociated through the formation of the bound state. This assumption can be checked by using other materials with different work functions. For example, tungsten is an interesting target material because it has the work function around -5 eV [60] for 1S-Ps, which is close to the difference of the binding energy between the 2P state. A new sample structure to be collided by 2P-Ps is necessary to be developed. Second, the large electric susceptibility of the P state could enhance interactions with the material in which the residual electric field is expected to exist. In this case, the 2S state which can be excited by two photon absorptions of 486 nm laser will have less decay rate. It is still challenging to induce the two photon absorptions inside the material because a high power and the good coherence are required: the Ps converter must be transparent enough to be put in an optical resonator which accumulates the laser power, or the more powerful laser by around 10 times than the adopted one in the present work is required.

4.4.3 Outlook for the rapid cooling of Ps

One of the straightforward directions to realize the rapid cooling is to modify the surface structure of pores such that abnormal phenomena are suppressed. For example, the broadening will be eased by removing dielectric groups or covering pores' surface by a metal layers so that the residual electric field in the pores will be quenched. Furthermore, covering of the surface by appropriate materials could alter the interaction between the surface and 2P-Ps into a repulsive one to prevent 2P-Ps from being dissociated under the string influence from the material. It is important to systematically test effects by the modifications using various type of materials.

Another interesting direction is to adopt another type of a cavity such as a bubble of liquid helium. 1S-Ps is known to have a relatively long life time around 100 ns in liquid helium with forming a bubble [61, 62]. It was proposed that liquid helium can be a good medium of the cavity to realizing Ps-BEC [63] thanks to an expected rapid thermalization process under frequent interactions through the surface of the bubble. It is still challenging to combine liquid helium with a bunched positrons, which usually requires to be in a high vacuum system, but it will be beneficial to conduct spectroscopic measurements of Ps in the bubble, and compare the results with theoretical predictions in order to establish methods to measure phase space density of Ps as performed in this work.

Chapter 5

Conclusion

Details of the decay process of Ps in the 2P state were quantitatively studied to develop the Ps confining cavity for efficient cooling. The silica aerogel was used as the test sample which had the new feature that 1S-Ps was not strongly affected in it. By analyzing the data with the realistic model, the decay rate of 2P-Ps (Γ_2) was measured as large as 7 THz in maximum, and the corresponding probability to decay per a collision was calculated as in the order of unity. The enhanced decay which was observed only for 2P-Ps favors that some of the distinctive features of the 2P state, such as the small binding energy or the high electric susceptibility, are origins of the decay process. The resonance of the decay which were observed at around 0.06 eV for Ps kinetic energy suggests that the decay proceeds through forming the bound state with the material. The line width of Ps Lyman-α transition was as broad as 1 nm in FWHM irrelevant with Γ_2. This observation suggests that the broadening was from not only the natural line width of the decay but also an inhomogeneous broadening, which is possibly caused by the residual electric field in the pores.

Acknowledgements

Bibliography

[1] K. Shu, X. Fan, T. Yamazaki, T. Namba, S. Asai, K. Yoshioka, and M. Kuwata-Gonokami, "Study on cooling of positronium for Bose–Einstein condensation", Journal of Physics B: Atomic, Molecular and Optical Physics **49**, 104001 (2016).

[2] B. S. Cooper, J.-P. Boilot, C. Corbel, F. Guillemot, L. Gurung, L. Liszkay, and D. B. Cassidy, "Annihilation of positronium atoms confined in mesoporous and macroporous SiO_2 films", Phys. Rev. B **97**, 205302 (2018).

[3] S. G. Karshenboim, "Precision physics of simple atoms: QED tests, nuclear structure and fundamental constants", Phys. Rep. **422**, 1 (2005).

[4] Y. Kataoka, S. Asai, and T. Kobayashi, "First test of $O(\alpha^2)$ correction of the orthopositronium decay rate", Physics Letters B **671**, 219 (2009).

[5] A. H. Al-Ramadhan and D. W. Gidley, "New precision measurement of the decay rate of singlet positronium", Phys. Rev. Lett. **72**, 1632 (1994).

[6] A. I. Mil'shtein and I. B. Khriplovich, "Large relativistic corrections to the positronium decay probability", Journal of Experimental and Theoretical Physics **79**, 379 (1994).

[7] G. Adkins, A. Salahuddin, and K. Schalm, "Order-α corrections to the decay rate of orthopositronium in the Fried-Yennie gauge", Physical Review A **45**, cited By 27, 7774 (1992).

[8] A. Ishida, T. Namba, S. Asai, T. Kobayashi, H. Saito, M. Yoshida, K. Tanaka, and A. Yamamoto, "New precision measurement of hyperfine splitting of positronium", Phys. Lett. B **734**, 338 (2014).

[9] M. S. Fee, S. Chu, A. P. Mills, R. J. Chichester, D. M. Zuckerman, E. D. Shaw, and K. Danzmann, "Measurement of the positronium 1^3S_1–2^3S_1 interval by continuous-wave two-photon excitation", Phys. Rev. A **48**, 192 (1993).

[10] G. S. Adkins, M. Kim, C. Parsons, and R. N. Fell, "Three-photon-annihilation contributions to positronium energies at order $m\alpha^7$", Phys. Rev. Lett. **115**, 233401 (2015).

[11] T. Yamazaki, T. Namba, S. Asai, and T. Kobayashi, "Search for CP violation in positronium decay", Phys. Rev. Lett. **104**, 083401 (2010).

[12] S. Asai, S. Orito, K. Yoshimura, and T. Haga, "Search for long-lived neutral bosons in orthopositronium decay", Phys. Rev. Lett. **66**, 2440 (1991).

[13] C. Vigo, L. Gerchow, L. Liszkay, A. Rubbia, and P. Crivelli, "First search for invisible decays of orthopositronium confined in a vacuum cavity", Phys. Rev. D **97**, 092008 (2018).

[14] A. Badertscher, P. Crivelli, W. Fetscher, U. Gendotti, S. N. Gninenko, V. Postoev, A. Rubbia, V. Samoylenko, and D. Sillou, "Improved limit on invisible decays of positronium", Phys. Rev. D **75**, 032004 (2007).

[15] A. Ore and J. L. Powell, "Three-photon annihilation of an electron-positron pair", Phys. Rev. **75**, 1696 (1949).

[16] P. A. M. Dirac, "On the annihilation of electrons and protons", Mathematical Proceedings of the Cambridge Philosophical Society **26**, 361 (1930).

[17] A. I. Alekseev, "Two-photon annihilation of positronium in the p-state", Journal of Experimental and Theoretical Physics **34**, 826 (1958).

[18] A. I. Alekseev, "Three-photon annihilation of positronium in the p-state", Journal of Experimental and Theoretical Physics **36**, 1312 (1959).

[19] Y. Nagashima, Y. Morinaka, T. Kurihara, Y. Nagai, T. Hyodo, T. Shidara, and K. Nakahara, "Origins of positronium emitted from SiO_2", Phys. Rev. B **58**, 12676 (1998).

[20] K. Ito, H. Nakanishi, and Y. Ujihira, "Extension of the equation for the annihilation lifetime of ortho-positronium at a cavity larger than 1 nm in radius", The Journal of Physical Chemistry B **103**, 4555 (1999), eprint: `https://doi.org/10.1021/jp9831841`.

[21] K. Wada and T. Hyodo, "A simple shape-free model for pore-size estimation with positron annihilation lifetime spectroscopy", Journal of Physics: Conference Series **443**, 012003 (2013).

[22] D. W. Gidley, W. E. Frieze, T. L. Dull, A. F. Yee, E. T. Ryan, and H.-M. Ho, "Positronium annihilation in mesoporous thin films", Phys. Rev. B **60**, R5157 (1999).

[23] T. L. Dull, W. E. Frieze, D. W. Gidley, J. N. Sun, and A. F. Yee, "Determination of pore size in mesoporous thin films from the annihilation lifetime of positronium", J. Phys. Chem. B **105**, 4657 (2001).

[24] H. Saito and T. Hyodo, "Quenching of positronium by surface paramagnetic centers in ultraviolet- and positron-irradiated fine oxide grains", Phys. Rev. B **60**, 11070 (1999).

[25] D. B. Cassidy, K. T. Yokoyama, S. H. M. Deng, D. L. Griscom, H. Miyadera, H. W. K. Tom, C. M. Varma, and A. P. Mills, "Positronium as a probe of transient paramagnetic centers in $a-SiO_2$", Phys. Rev. B **75**, 085415 (2007).

[26] B. S. Cooper, A. M. Alonso, A. Deller, L. Liszkay, and D. B. Cassidy, "Positronium production in cryogenic environments", Phys. Rev. B **93**, 125305 (2016).

[27] Y. Nagashima, M. Kakimoto, T. Hyodo, K. Fujiwara, A. Ichimura, T. Chang, J. Deng, T. Akahane, T. Chiba, K. Suzuki, B. T. A. McKee, and A. T. Stewart, "Thermalization of free positronium atoms by collisions with silica-powder grains, aerogel grains, and gas molecules", Phys. Rev. A **52**, 258 (1995).

[28] A. Ishida, K. Shu, T. Murayoshi, X. Fan, T. Namba, S. Asai, K. Yoshioka, M. Kuwata-Gonokami, N. Oshima, B. E. O'Rourke, and R. Suzuki, "Study on positronium Bose–Einstein condensation", JJAP Conference Proceedings **011001**, 7 (2018).

[29] K. Shu, A. Ishida, T. Namba, S. Asai, N. Oshima, B. E. O'Rourke, and K. Ito, "Observation of *ortho*–positronium thermalization at cryogenic temperatures", In preparation.

[30] P. Crivelli, C. Cesar, and U. Gendotti, "Advances towards a new measurement of the 1S-2S transition of positronium", Canadian Journal of Physics **89**, 29 (2011).

[31] D. A. Cooke, P. Crivelli, J. Alnis, A. Antognini, B. Brown, S. Friedreich, A. Gabard, T. W. Haensch, K. Kirch, A. Rubbia, and V. Vrankovic, "Observation of positronium annihilation in the 2S state: towards a new measurement of the 1S-2S transition frequency", Hyperfine Interactions **233**, 67 (2015).

[32] M. Tanabashi et al. (Particle Data Group), "Review of particle physics", Phys. Rev. D **98**, 030001 (2018).

[33] M. Villata, "CPT symmetry and antimatter gravity in general relativity", EPL (Europhysics Letters) **94**, 20001 (2011).

[34] D. J. Cross, *Response to "CPT symmetry and antimatter gravity in general relativity"*, 2011, arXiv:1108.5117 [gr-qc].

[35] M. Villata, "Reply to "Comment to a paper of M. Villata on antigravity"", Astrophysics and Space Science **337**, 15 (2012).

[36] P. M. Platzman and A. P. Mills, "Possibilities for Bose condensation of positronium", Phys. Rev. B **49**, 454 (1994).

[37] O. Morandi, P.-A. Hervieux, and G. Manfredi, "Bose–Einstein condensation of positronium in silica pores", Phys. Rev. A **89**, 033609 (2014).

[38] D. W. Fitzakerley, M. C. George, E. A. Hessels, T. D. G. Skinner, C. H. Storry, M. Weel, G. Gabrielse, C. D. Hamley, N. Jones, K. Marable, E. Tardiff, D. Grzonka, W. Oelert, and M. Zielinski (ATRAP Collaboration), "Electron-cooled accumulation of 4×10^9 positrons for production and storage of antihydrogen atoms", Journal of Physics B: Atomic, Molecular and Optical Physics **49**, 064001 (2016).

[39] D. B. Cassidy, S. H. M. Deng, R. G. Greaves, and A. P. Mills, "Accumulator for the production of intense positron pulses", Review of Scientific Instruments **77**, 073106 (2006).

[40] N. Oshima, R. Suzuki, T. Ohdaira, A. Kinomura, T. Narumi, A. Uedono, and M. Fujinami, "Brightness enhancement method for a high-intensity positron beam produced by an electron accelerator", Journal of Applied Physics **103**, 094916 (2008).

[41] N. Oshima, R. Suzuki, T. Ohdaira, A. Kinomura, T. Narumi, A. Uedono, and M. Fujinami, "Development of positron microbeam in AIST", Materials Science Forum **607**, 238 (2008).

[42] D. B. Cassidy and A. P. Mills, "Physics with dense positronium", physica status solidi (c) **4**, 3419 (2007).

[43] V. Vanyashin, "Coherent decay of positronium Bose condensate", Letters in Mathematical Physics **31**, 143 (1994).

[44] H. K. Avetissian, A. K. Avetissian, and G. F. Mkrtchian, "Self-amplified gamma-ray laser on positronium atoms from a Bose-Einstein condensate", Phys. Rev. Lett. **113**, 023904 (2014).

[45] D. B. Cassidy, M. W. J. Bromley, L. C. Cota, T. H. Hisakado, H. W. K. Tom, and A. P. Mills, "Cavity induced shift and narrowing of the positronium Lyman-α transition", Phys. Rev. Lett. **106**, 023401 (2011).

[46] R. H. Dicke, "The effect of collisions upon the Doppler width of spectral lines", Phys. Rev. **89**, 472 (1953).

[47] T. Hyodo, K. Wada, A. Yagishita, T. Kosuge, Y. Saito, T. Kurihara, T. Kikuchi, A. Shirakawa, T. Sanami, M. Ikeda, S. Ohsawa, K. Kakihara, and T. Shidara, "KEK-IMSS slow positron facility", Journal of Physics: Conference Series **262**, 012026 (2011).

[48] A. Burgess, "Tables of hydrogenic photoionization cross-sections and recombination coefficients", Memoirs of the Royal Astronomical Society **69**, 1 (1965).

[49] Y. Huang, J. Chang, Y. Cheng, Z. Chen, J. Hu, X. Ji, F. Li, J. Li, Q. Li, X. Qian, S. Jetter, W. Wang, Z. Wang, Y. Xu, and Z. Yu, "The Flash ADC system and PMT waveform reconstruction for the Daya Bay experiment", Nuclear Instruments and Methods in Physics Research Section A: Accelerators, Spectrometers, Detectors and Associated Equipment **895**, 48 (2018).

[50] A. Deller, "SSPALS: A tool for studying positronium", Nuclear Instruments and Methods in Physics Research Section A: Accelerators, Spectrometers, Detectors and Associated Equipment **922**, 91 (2019).

[51] R. Loudon, *The quantum theory of light* (OXFORD SCIENCE PUBLICATIONS, 2000).

[52] Y. Kataoka, "Test of bound state qed higher order correction: precision measurement of orthopositronium decay rate", PhD thesis (The University of Tokyo, 2007).

[53] Nippon Aerosil Co. Ltd., *AEROSIL – Fumed Silica*.

[54] S. Villalba, H. Failache, A. Laliotis, L. Lenci, S. Barreiro, and A. Lezama, "Rb optical resonance inside a random porous medium", Opt. Lett. **38**, 193 (2013).

[55] R. OHTA, Y. UENO, and K. AJITO, "Raman spectroscopy of pharmaceutical cocrystals in nanosized pores of mesoporous silica", Analytical Sciences **33**, 47 (2017).

[56] C. M. Surko, G. F. Gribakin, and S. J. Buckman, "Low-energy positron interactions with atoms and molecules", Journal of Physics B: Atomic, Molecular and Optical Physics **38**, R57 (2005).

[57] S. J. Tao, S. Y. Chuang, and J. Wilkenfeld, "Positron annihilation in nitric oxide and nitrogen dioxide", Phys. Rev. A **6**, 1967 (1972).

[58] S. Y. Chuang and S. J. Tao, "Quenching of positronium in nitrogen dioxide", Phys. Rev. A **9**, 989 (1974).

[59] T. Hyodo, T. Nakayama, H. Saito, F. Saito, and K. Wada, "The quenching of ortho - positronium", physica status solidi c **6**, 2497 (2009).

[60] H. Terabe, S. Iida, K. Wada, T. Hyodo, A. Yagishita, and Y. Nagashima, "Efficient emission of positronium atoms from an Na-coated polycrystalline tungsten surface", Journal of Physics: Conference Series **443**, 012075 (2013).

[61] D. A. L. Paul and R. L. Graham, "Annihilation of positrons in liquid helium", Phys. Rev. **106**, 16 (1957).

[62] J. Wackerle and R. Stump, "Annihilation of positrons in liquid helium", Phys. Rev. **106**, 18 (1957).

[63] A. P. Mills, "Positronium Bose-Einstein condensation in liquid ^{4}He bubbles", Phys. Rev. A **100**, 063615 (2019).